The Astronomical Journal, 135:2470–2495, 2008 June doi:10.1088/0004-6256/135/6/2470

RADIO OBSERVATIONS OF THE HUBBLE DEEP FIELD–SOUTH REGION. IV. OPTICAL PROPERTIES OF THE FAINT RADIO POPULATION

Minh T. Huynh[1], Carole A. Jackson[2], Ray P. Norris[2], and Alberto Fernandez-Soto[3]
[1] Spitzer Science Center, MS220-6, California Institute of Technology, Pasadena, CA 91125, USA; mhuynh@ipac.caltech.edu
[2] Australia Telescope National Facility, CSIRO Radiophysics Laboratory, P.O. Box 76, Epping, NSW 2121, Australia
[3] Grupo de Radioastronomía, Dept. Astronomia, Universitat de Valencia. Av. Dr. Moliner 50, Burjassot, 46100-Valencia, Spain
Received 2007 October 19; accepted 2008 March 21; published 2008 May 15

ABSTRACT

The Australia Telescope Hubble Deep Field–South (ATHDF-S) survey of the Hubble Deep Field–South (HDF-S) reaches sensitivities of ∼10 μJy at 1.4, 2.5, 5.2, and 8.7 GHz, making the ATHDF-S one of the deepest surveys ever performed with the Australia Telescope Compact Array (ATCA). Here, we present the optical identifications of the ATHDF-S radio sources using data from the literature. We find that ∼66% of the radio sources have optical counterparts to $I = 23.5$ mag. Deep *Hubble Space Telescope* (*HST*) imaging of the area identifies a further 12% of radio sources. We present new spectroscopic observations for 98 of the radio sources and supplement these spectroscopic redshifts with photometric ones calculated from five-band optical imaging. The host galaxy colors and radio-to-optical ratios indicate that low-luminosity (or "radio-quiet") active galactic nuclei make up a significant proportion of the sub-mJy radio population, a result which is in accordance with a number of other deep radio studies. The radio-to-optical ratios of the bright ($S_{1.4\,\mathrm{GHz}} > 1$ mJy) sources are consistent with a bimodal distribution.

Key words: radio continuum: galaxies – surveys

Online-only material: color figures, machine-readable tables

1. INTRODUCTION

Many massive galaxies in the local universe harbor a supermassive black hole, and this implies that most, if not all, galaxies hosted an active galactic nucleus (AGN) at some point in time (Kormendy & Richstone 1995). It is now thought that star formation and AGNs are linked by some mechanism collectively known as "AGN-driven feedback" (e.g. Croton et al. 2006). Radio emission can be produced by both AGN and star-forming processes, and thus radio surveys provide a unique window to study the cosmic evolution of both these important processes.

Early radio surveys ($S_{1.4\,\mathrm{GHz}} \gtrsim 100$ mJy) found objects with powerful radio emitting jets, which are generally termed "radio-loud" AGNs. Recent deep radio surveys have found that the Euclidean-normalized radio source counts flatten below about 1 mJy and this cannot be explained by a population of radio-loud AGNs. A nonevolving population of local ($z < 0.1$) low-luminosity radio galaxies (Wall et al. 1986), strongly evolving normal spirals (Condon 1984, 1989), and starburst galaxies (Windhorst et al. 1985; Rowan-Robinson et al. 1993) have all been suggested to explain this new population. The faint radio source counts have been successfully modeled by star-forming galaxies (Seymour et al. 2004; Huynh et al. 2005). However, it has also been shown that low-luminosity radio-quiet AGNs can also contribute to the flattening of the source count at sub-mJy levels (Jarvis & Rawlings 2004).

It is now clear that the sub-mJy population is made up of *both* star-forming galaxies and low-luminosity AGNs, but surprisingly little is known about the exact mix. This is because the optical counterparts to the radio sources are faint and hence spectroscopic follow-up is difficult and/or requires massive amounts of telescope time. Pioneering work in the Hubble Deep Field–North (HDF-N) by Richards et al. (1999) found that roughly 60% of sub-mJy ($S_{1.4\,\mathrm{GHz}} > 0.04$ mJy) sources are associated with bright ($I \sim 22$) disk galaxies, 20% are low-luminosity AGNs, and the remaining 20% have no counterpart brighter than $I = 25$. Deep Advanced Camera for Surveys (ACS) imaging ($i_{775} < 27$) of the Great Observatories Origins Deep Survey (GOODS) South field identified optical counterparts to 90% of the faint ($S_{1.4\,\mathrm{GHz}} > 0.06$ mJy) radio sources, and about 60% of the GOODS radio sources with spectroscopic information have a spectrum consistent with star-formation processes (Afonso et al. 2006). Simpson et al. (2006) find that 90% of $S_{1.4\,\mathrm{GHz}} > 0.1$ mJy radio sources are identified to $R \sim 27$ in the Subaru/*XMM-Newton* Deep Field and show that faint and bright radio sources have similar optical colors. This suggests that many of the faint radio sources are passively evolving ellipticals. Using a highly spectroscopically complete (70%) sample of faint radio sources in the HDF-N, Barger et al. (2007) confirmed that the optical hosts do not vary much with redshift or radio flux density. The optical host properties, coupled with X-ray information, provide evidence for a significant proportion of low-luminosity or obscured AGNs in the faint radio source population (Simpson et al. 2006; Barger et al. 2007). Recent work using radio-based properties, such as morphology, the near-IR-to-radio flux density ratio, the mid-IR-to-radio flux density ratio, and radio luminosity, has found that AGNs still contribute a third of the total 1.4 GHz source counts at the faintest flux densities (∼50 μJy) (Seymour et al. 2004).

The Hubble Deep Field–South (HDF-S) is an ideal field for studying radio sources because of the wealth of publicly available data. This field has been studied in wavelengths from the radio to UV optical, and spectroscopic and photometric redshifts are available for thousands of galaxies in the HDF-S and surrounding regions (Teplitz et al. 2001; Rudnick et al. 2001; Labbé et al. 2003).

Radio observations of the HDF-S were made between 1998 and 2001 with the Australia Telescope Compact Array (ATCA) using all four available frequency bands. Between 100 and 300 h of observing at each band yielded images at 1.4, 2.5, 5.2, and 8.7 GHz with maximum sensitivities of ∼10 μJy root mean square (rms). A detailed description of the observations, data

reduction, and initial results was given by Norris et al. (2005) (hereafter Paper I). The full 1.4 GHz catalog and radio source counts were presented in Huynh et al. 2005 (hereafter Paper II). The 2.5, 5.2, and 8.7 GHz catalogs were presented in Huynh et al. (2007a) (hereafter Paper III).

In this paper, we present the optical properties of the Australia Telescope Hubble Deep Field–South (ATHDF-S) radio sources. This paper is organized as follows. In Section 2, we summarize the existing radio and optical images and present the optical counterparts to the ATHDF-S radio sources. Spectroscopic observations by our team and others are presented in Section 3. In Section 4, we present the photometric redshifts derived from the optical imaging. We discuss the photometric properties of the faint radio population in Section 5.

We assume a Hubble constant of 71 km s^{-1} Mpc^{-1}, $\Omega_M = 0.27$, and $\Omega_\Lambda = 0.73$ throughout this paper.

2. IMAGING DATA

2.1. Radio

The radio observations and data reduction are detailed in Papers I–III, but here we provide a brief summary. The observations consist of single pointings centered on right ascension (R.A.) = 22 33 25.96, declination (decl.) = −60 38 09.0 (J2000.0) (1.4 and 2.5 GHz), and R.A. = 22 32 56.22, decl. = −60 33 02.7 (J2000.0) (5.2 and 8.7 GHz). The 5.2 and 8.7 GHz observations are centered on the *Hubble Space Telescope* (*HST*) Wide Field Planetary Camera (WFPC) field, while the 1.4 and 2.5 GHz observations were pointed halfway between the WFPC field and a bright confusing source to allow the bright source to be well cleaned from the 1.4 and 2.5 GHz images.

We used a wide variety of ATCA configurations to maximize the u–v coverage. The correlator was set to continuum mode (2 × 128 MHz bandwidth), with each 128 MHz bandwidth divided into 32 × 4 MHz channels. The primary flux density calibrator is PKS B1934-638, while secondary gain and phase calibrations were taken throughout our observations using both PKS B2205-636 and PKS B2333-528.

The final images have a maximum sensitivity of 11.0, 10.4, 7.8, and 11.0 μJy rms at 1.4, 2.5, 5.2, and 8.7 GHz, respectively. The size of the images varies because the primary beam of the ATCA is smaller at high frequencies. We cataloged 1.4 GHz sources to 20 arcmin distance from the image center, while for 8.7 GHz we reach 3.5 armin distance. Sources were cataloged to a local signal-to-noise ratio (S/N) of 5σ at 1.4, 5.2, and 8.7 GHz, and 5.5σ at 2.5 GHz. A consolidated catalog with the radio sources matched across all four bands was presented in Paper III, comprising 473 individual sources.

2.2. CTIO Wide Field Images

Palunas et al. (2000) observed the HDF-S region using the Big Throughput Camera (BTC) on the Cerro Tololo Inter-American Observatory (CTIO) 4 m during 1998 September. Images were taken in the Sloan Digital Sky Survey (SDSS) u, Johnson B and V, and Cousins R and I filters. The BTC has a pixel size of 0.43 arcsec and covers a total area of 34.8 × 34.8 arcmin. Individual exposures were dithered during the observations to fill in the gaps between the BTC CCDs. This resulted in a contiguous field of approximately 44 × 44 arcmin, centered on the main HDF-S.

Catalogs of individual sources were compiled by Palunas et al. (2000) using Source Extractor (SExtractor) (Bertin & Arnouts 1996). Palunas et al. (2000) fix their photometric system to the Johnson UBV and Cousins RI system (Landolt 1992). The sensitivity of the images differ, with the 5σ detection limits for point-like objects in each band range quoted as $24 < u < 25$, $25.6 < B < 26.6$, $25 < V < 26$, $25 < R < 25.8$, and $23.5 < I < 24.4$. About 50% of the area of each image has a sensitivity limit at the bright end of the range.

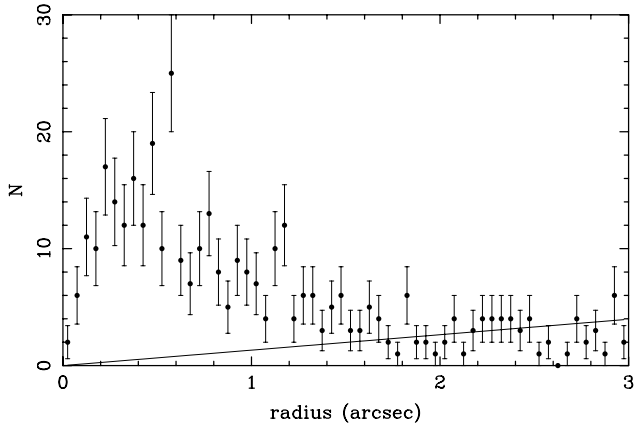

Figure 1. Number of candidate CTIO counterparts of ATHDF-S sources as a function of radio-to-optical offset. The solid line shows the number of chance coincidences expected from the CTIO source density of 70 409 objects in a 0.588 square degree region.

We cross-matched the combined ATHDF-S catalog (Paper III) against the CTIO wide field images. To aid in choosing a matching radius we plot the number of candidate matches and the number of chance coincidences against radio-optical offset in Figure 1. Here the number of chance coincidences is determined from the CTIO source density (70,409 cataloged sources over 0.588 deg^2). Figure 1 shows that the number of chance coincidences matches the number of candidates at a radius of 1.8 arcsec. We therefore choose this distance to be our matching radius.

For the worst-case scenario of S/N = 5 and seeing of 2 arcsec FWHM, we estimate the 1σ CTIO positional uncertainty to be $\sim 0.4''$ in each coordinate. This is similar in scale to the CTIO pixel size. In the ATHDF-S, at 1.4 GHz, the average uncertainty is 0.36″ and 0.43″ in R.A. and decl., respectively. We thus expect the offsets between our radio positions and the CTIO positions to have an rms value of approximately $\sqrt{0.4^2 + 0.4^2} = 0.6''$ in each coordinate, neglecting any offsets between the coordinate frames. Figure 2 shows the offsets between the radio and optical positions, which indicates there is a possible R.A. offset in the ATHDF-S and CTIO image coordinates of $\leqslant$0.5 arcsec. For probable matches closer than 2 arcsec, the mean offset in R.A., δR.A., is −0.11 arcsec and the rms is 0.56 arcsec, where $\delta\text{R.A.} = \text{R.A.}_{\text{ATHDF-S}} - \text{R.A.}_{\text{CTIO}}$. Similarly, the mean offset in decl. is −0.03 arcsec, with an rms of 0.60 arcsec. We correct for the coordinate shifts between the ATHDF-S and CTIO images by shifting the CTIO positions by these mean offsets in R.A. and decl. before the final matching. The mean offset in R.A. and decl. after shifting the CTIO coordinates is −0.02 and 0.00 arcsec, respectively, with rms values of 0.56 and 0.64 arcsec (Figure 3). This agrees well with the above predicted rms of 0.6″ in each coordinate. Our matching radius of 1.8 arcsec is equivalent to about 2.2σ, and so should include ∼97% of the true identifications.

The I-band CTIO image was examined at all radio positions. In 11 cases the optical counterpart is close to a bright star, so

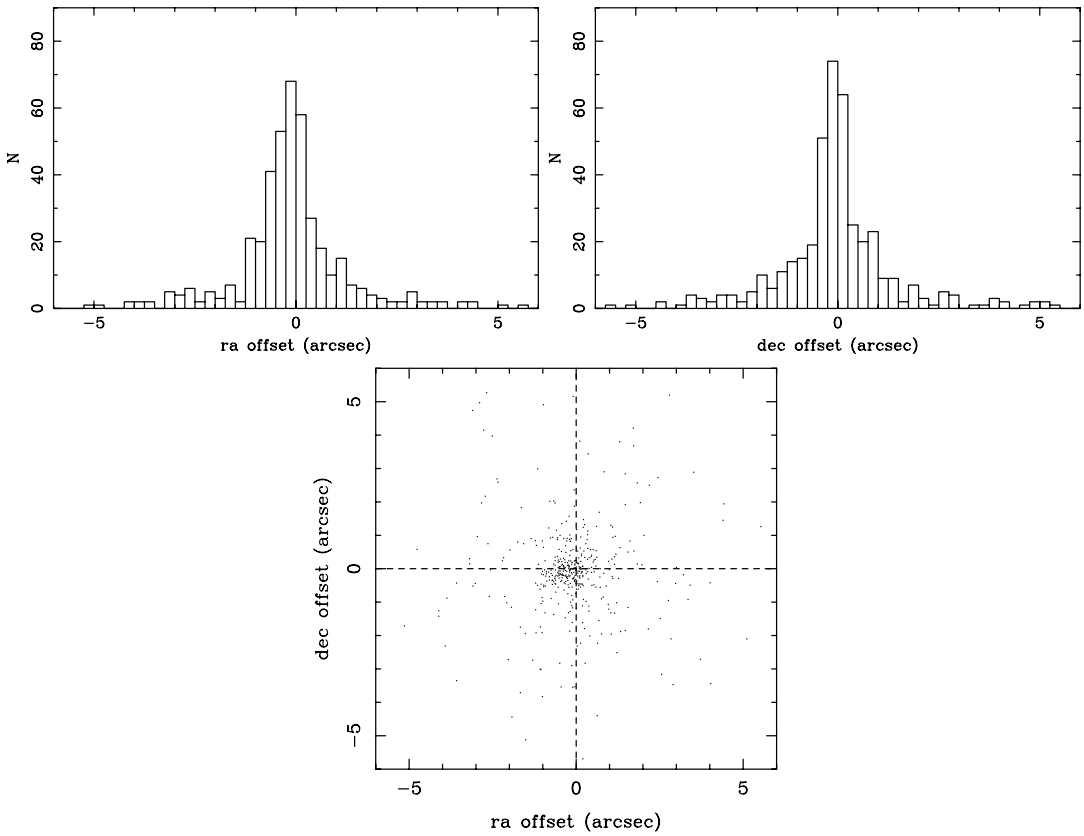

Figure 2. Radio-to-optical position offsets, uncorrected for offset between CTIO and ATHDF-S images. Bottom panel: distribution of the offsets between the radio and optical positions for all ATHDF-S and CTIO sources closer than 6 arcsec. Top panel: distribution of the offset in R.A. and decl. for the CTIO sources closer than 6 arcsec.

the photometry for these sources is not reliable. These instances are flagged in the catalog. For radio sources which comprise a multiple component radio source (see Paper II) the optical counterpart may be positioned between the two or more sources, i.e. at the radio centroid. The two cases where this occurred (multiple sources ATHDF-S_J223232.4−603542 and ATHDF-S_J223443.9−602739) are shown in Figure 4.

The number of ATHDF-S sources with a CTIO optical counterpart is 306. Eight of the radio sources lie outside of the CTIO image area, so out of a possible 465 radio sources, 66% have optical counterparts in the CTIO images. We expect 44 chance coincidences using the CTIO source density of 119,740 deg^{-2} and a total search area of $(\pi * 1.8'^2) \times 473$. To derive another estimate of the number of chance coincidences we shifted the radio source positions north by 0.5 arcmin and re-applied the matching program. From this method we find 55 chance coincidences, which is consistent with our first estimation. We therefore conclude that up to 50/315, or 16%, of our CTIO matches could be spurious.

The results of cross-matching the full ATHDF-S catalog against the CTIO imaging are presented in Table 1. A description of Table 1 is as follows:

Column 1: ATHDF-S source name.
Column 2: CTIO flag. "YES" indicates there is a CTIO counterpart within the 1.8 arcsec matching radius. "NO" means there is no CTIO counterpart within the 1.8 arcsec matching radius. "S" indicates there is a nearby bright star which may affect the photometry. "OUT" indicates that the source lies outside of the CTIO images.
Column 3: CTIO source ID, corresponding to the source number from the CTIO catalog (P. Palunas et al. 2008, submitted).
Column 4: *U* magnitude.
Column 5: rms error in *U* magnitude.
Column 6: *B* magnitude.
Column 7: rms error in *B* magnitude.
Column 8: *V* magnitude.
Column 9: rms error in *V* magnitude.
Column 10: *R* magnitude.
Column 11: rms error in *R* magnitude.
Column 12: *I* magnitude.
Column 13: rms error in *I* magnitude.
Column 14: CTIO photometric redshift.
Column 15: CTIO photometric redshift uncertainty.

2.3. *Hubble Space Telescope Images*

Images of the HDF-S were obtained by all three instruments on board the *HST* in 1998: the Wide Field Planetary Camera 2 (WFPC2), the Near-Infrared Camera and Multi-Object Spectrograph (NICMOS), and the Space Telescope Imaging Spectrograph (STIS). The *HST* observing strategy is described in Williams et al. (2000).

2.3.1. *Main Fields*

The main deep field WFPC2 observations were centered on R.A. = 22 32 56.22, and decl. = −60 33 02.69 (J2000). The WFPC2 observations consist of exposures in four broadband filters: F300W, F450W, F606W, and F814W, which have central

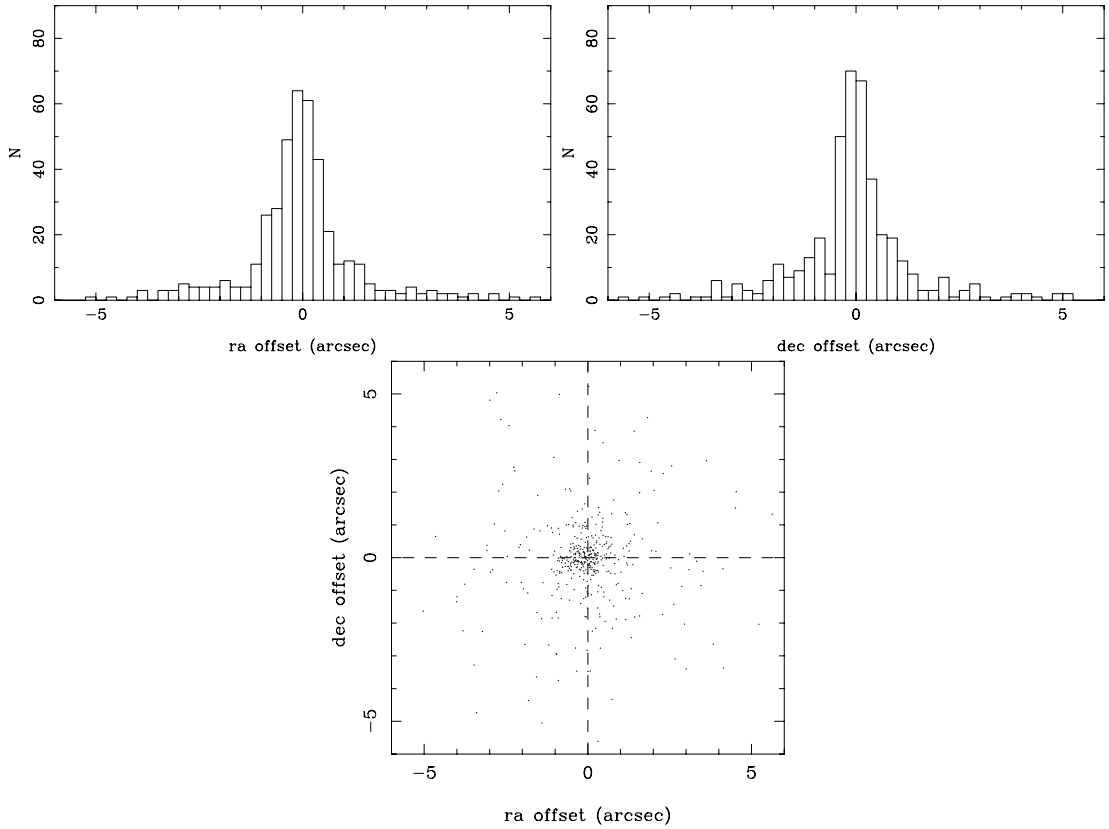

Figure 3. Radio-to-optical position offsets, with CTIO coordinates shifted to correct for offset between CTIO and ATHDF-S images. Bottom panel: distribution of the offsets between the radio and optical positions for all ATHDF-S and CTIO sources closer than 6 arcsec. Top panel: distribution of the offset in R.A. and decl. for the CTIO sources closer than 6 arcsec.

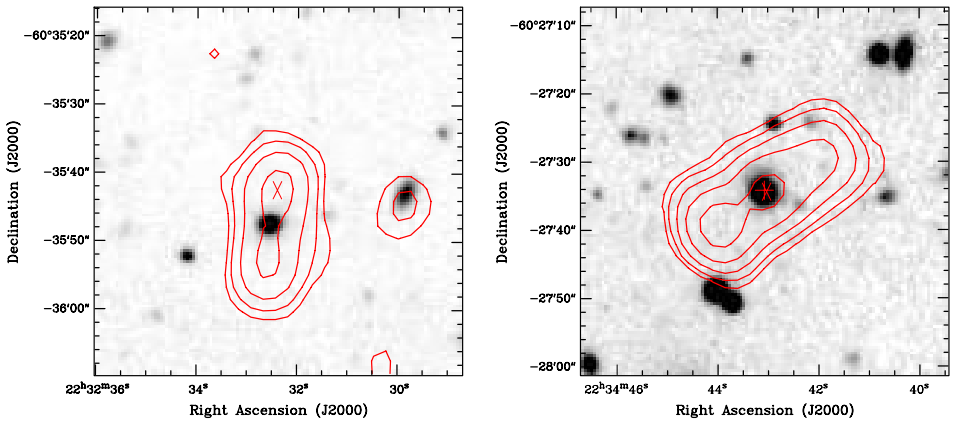

Figure 4. Postage stamp images for radio sources with multiple components. The optical counterparts are clearly positioned between the two or more radio source components. The gray-scale images are CTIO *I*-band images and the contours are 1.4 GHz flux densities, set at 5, 10, 20, 50, 100, and 200σ. Left: multiple radio source ATHDF-S_J223232.4−603542. Right: multiple radio source ATHDF-S_J223443.9−602739.

(A color version of this figure is available in the online journal)

wavelengths of approximately 2940, 4520, 5940, and 7920 Å, respectively. These filters are the *HST* analogs of the well-known Johnson U, B, V, and Cousins I filters. The 10σ limiting AB magnitude of the WFPC2 observations are 26.8, 27.7, 28.3, and 27.7 for the F300W, F450W, F606W, and F814W filters, respectively (Casertano et al. 2000).

The NICMOS instrument was used to obtain deep near infrared (IR) images. Imaging was performed in three NICMOS filters (Williams et al. 2000): F110W, F160W and F222W. These filters correspond roughly to J (F110W), H (F160W), and K (F222W). The NICMOS field is centered at R.A. = 22 32 51.75, and decl. = −60 38 48.20 (J2000). The sensitivity, while not uniform over the whole image, reaches a limiting F160W (H) AB magnitude of ≡28.7 and F222W (K) AB magnitude of ≡24.8 (Yahata et al. 2000).

The STIS observations were centered on the STIS QSO (Sealey et al. 1998) at R.A. = 22 33 37.5883, and decl. = −60 33 29.128 (J2000). The imaging was performed mainly with the 50CCD detector in a filterless mode which provides a wide (2500 Å FWHM) bandpass centered at approximately

Table 1
CTIO Properties of the Cataloged ATHDF-S Sources

ATHDF-S name	CTIO flag	CTIO ID	U mag	U rms error	B mag	B rms error	V mag	V rms error	R mag	R rms error	I mag	I rms error	CTIO phot z	CTIO phot z uncertainty
ATHDFS_J223314.6-605543	YES	2689	18.11	0.01	18.05	0.00	17.42	0.00	16.98	0.00	16.52	0.01	0.01	0.05
ATHDFS_J223316.9-605533	YES	3290	17.13	0.01	16.88	0.00	15.96	0.00	15.37	0.00	14.72	0.00	0.17	0.11
ATHDFS_J223353.9-605452	YES	1648	22.99	0.16	24.05	0.18	23.00	0.15	22.41	0.12	21.23	0.19	0.98	0.25
ATHDFS_J223334.6-605455	NO	...	...	...	...	...	...	...	...	...	...	...	...	...
ATHDFS_J223214.8-605430	YES	2073	23.10	0.16	23.74	0.12	22.67	0.08	22.28	0.09	21.58	0.22	0.27	0.18
ATHDFS_J223448.4-605417	YES	2430	23.48	0.50	24.58	0.61	24.31	0.82	22.89	0.42	22.11	0.94	0.71	0.35
ATHDFS_J223317.5-605416A	NO	...	...	...	...	...	...	...	...	...	...	...	...	...
ATHDFS_J223317.5-605416B	NO	...	...	...	...	...	...	...	...	...	...	...	...	...
ATHDFS_J223156.0-605417	NO	...	...	...	...	...	...	...	...	...	...	...	...	...
ATHDFS_J223204.8-605414	YES	2735	20.14	0.02	20.52	0.01	19.50	0.01	18.94	0.01	18.28	0.02	0.21	0.15

(This table is available in its entirety in a machine-readable form in the online journal. A portion is shown here for guidance regarding its form and content)

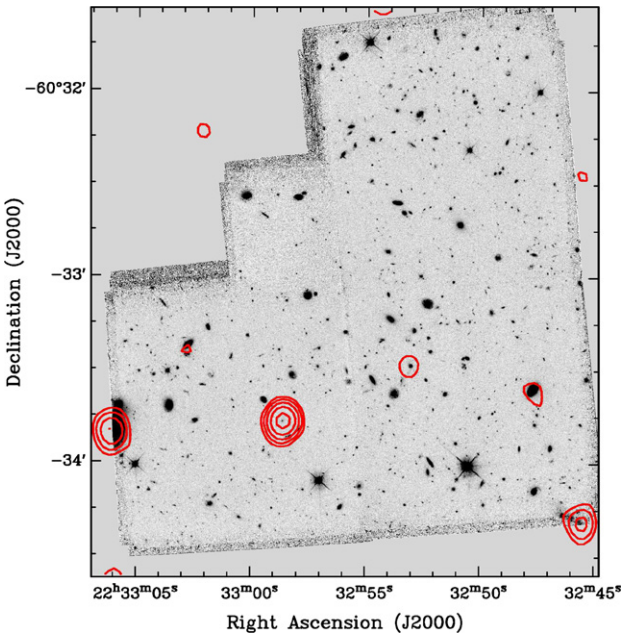

Figure 5. HDF-S main WFPC2 field—F814W image. The contours are 1.4 GHz flux densities, set at 5, 10, 20, 50, 100, and 200σ.
(A color version of this figure is available in the online journal)

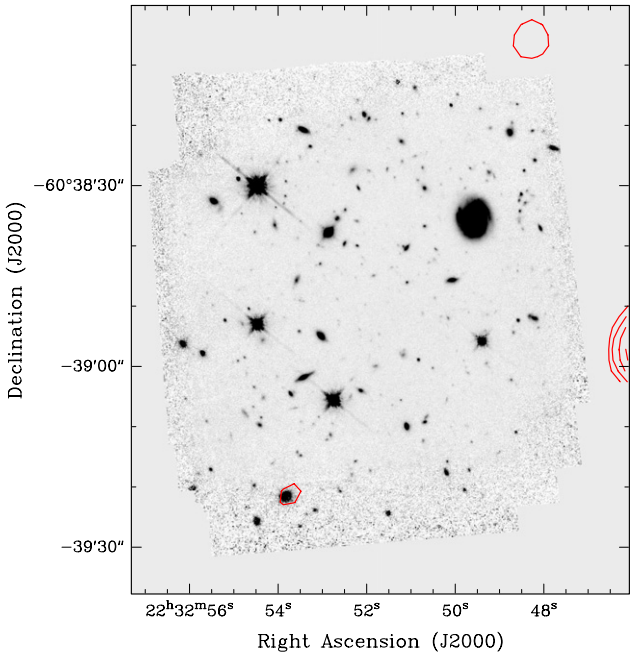

Figure 6. HDF-S main NICMOS field—F160W image. The contours are 1.4 GHz flux densities, set at 5, 10, 20, 50, 100, and 200σ.
(A color version of this figure is available in the online journal)

5800 Å. Rough color information was obtained by observations with the F28X50LP filter which is a long-pass filter beginning at approximately 5500 Å. These images cover a square region 0.83 arcmin^2 in total with a resolution of 0.05 per pixel. The filterless 50CCD images roughly correspond to $V + I$ and reach a depth of 29.4 AB magnitudes (Gardner et al. 2000).

Figures 5 to 7 show the full *HST* deep images overlaid with ATHDF-S 1.4 GHz contours. Four of the ATHDF-S radio sources lie within the WFPC2 field, one is in the NICMOS field, and two lie in the STIS field (Tables 2–4). All four sources within WFPC have a counterpart within 1.5 arcsec, and the others have counterparts within 0.5 arcsec. Using the WFPC2 source density of 2657 objects over 5.07 arcmin^2, we expect only one of these alignments, at most, is due to chance. The gray-scale postage stamp images of each source are presented in Figure 8 .

2.3.2. Flanking Fields

In addition to the main deep field exposures, a series of shallower observations were carried out over 27 orbits of the *HST*. Nine two-orbit WFPC2 pointings were used to observe a contiguous area of sky between the deep STIS, WFPC2, and NICMOS fields, overlapping both the STIS and NICMOS deep fields (Williams et al. 2000). Each of the WFPC2 flanking field exposures has simultaneous STIS and NICMOS exposures. The WFPC2 observations were performed in the I-band (F814W), while the STIS images were with the filterless 50CCD configuration and NICMOS images were in the H-band (F160W). While sensitivity varies slightly between the images, the average 5σ limiting AB magnitude for the flanking field images is I (F814W) = 26.02, H (F160W) = 26.32, and $V + I$ (50CCD) = 28.24 for the WFPC2, NICMOS, and STIS images, respectively (Lucas et al. 2003).

A deep nine-orbit STIS filterless 50CCD image of the main NICMOS field was also obtained as part of the flanking fields program. This was in order to obtain rough color information on NICMOS objects. The STIS image reaches a 5σ AB magnitude of $V+I$ = 29.09 (Lucas et al. 2003). Simultaneous exposures by WFPC2 achieve V (F606W) = 27.79 and I (F814W) = 27.15,

Table 2
Summary of WFPC2 Counterparts

ATHDF-S name	F300 magnitude	F300 rms error	F450 magnitude	F450 rms error	F606 magnitude	F606 rms error	F814 magnitude	F814 rms error	Morphological information
ATHDF-S_J223258.6−603346	27.53	0.68	28.48	0.77	27.05	0.13	25.12	0.04	No info
ATHDF-S_J223247.6−603337	22.70	0.02	21.69	0.00	20.55	0.00	19.55	0.00	Late-type spiral
ATHDF-S_J223253.1−603329	25.00	0.07	24.31	0.02	23.69	0.01	22.56	0.00	No info
ATHDF-S_J223302.8−603323	25.45	0.19	23.60	0.02	23.36	0.01	22.79	0.01	Barred spiral

Table 3
Summary of NICMOS Counterparts

ATHDF-S name	F110 magnitude	F110 rms error	F160 magnitude	F160 rms error	F222 magnitude	F222 rms error	Morphological information
ATHDF-S_J223253.7−603921	21.20	0.05	19.97	0.02	19.38	0.07	No info

Table 4
Summary of STIS Counterparts

ATHDF-S name	50ccd magnitude	50ccd rms error	lp magnitude	lp rms error	NUV magnitude	NUV rms error	FUV magnitude	FUV rms error	Morphological information
ATHDF-S_J223337.5−603329	17.83	0.0	17.48	0.00	...	...	29.13	0.00	Bright point source (STIS QSO)
ATHDF-S_J223339.4−603306	24.76	0.01	24.46	0.04	41.00	0.00	37.33	0.00	Irregular and disturbed, Possible merging system

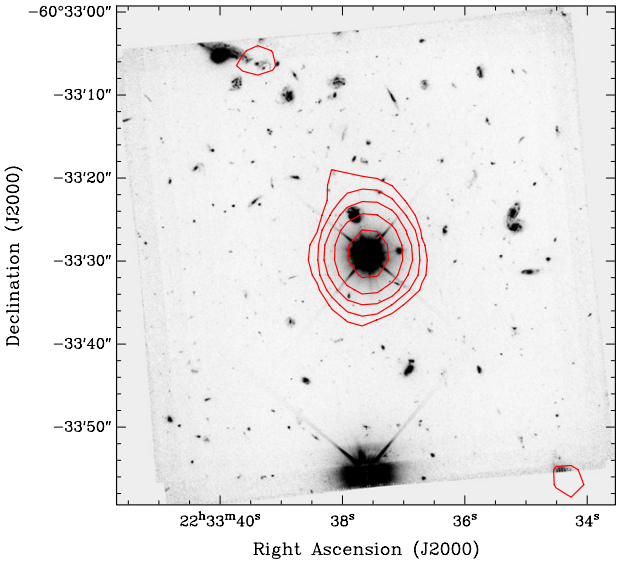

Figure 7. HDF-S main STIS field—50CCD image. The contours are 1.4 GHz flux densities, set at 5, 10, 20, 50, 100, and 200σ.

(A color version of this figure is available in the online journal)

and the simultaneous NICMOS imaging depth is J (F110W) = 26.94 and H (F160W) = 26.66 (Lucas et al. 2003).

We cross-matched the positions of our ATHDF-S radio sources with the full flanking field catalogs (Lucas et al. 2003). Flanking field objects were considered probable counterparts if the positional offset was less than three times the radio positional uncertainty. The largest offset accepted as a match is for ATHDF-S_J223307.1−603448, where the WFPC2 counterpart is radially offset from the radio position by 1.96″. In Table 5 we summarize the properties of the counterparts found in the STIS, NICMOS, and WFPC2 flanking fields, respectively. The gray-scale *HST* postage stamp images with overlaid radio contours for all flanking field counterparts are presented in Figures 9–11.

2.3.3. Analysis of HST Counterparts and Optically Faint Microjansky Sources

In Section 2.2, we found that 66% of our ATHDF-S sources are detected by CTIO imaging. In the main WFPC2 field, the *HST* imaging achieves sensitivities of 4.2 mag deeper than CTIO in the F814W (pseudo-I) band. In the flanking fields, the *HST* goes 2.5 mag deeper in I. Thus, we expect the *HST* imaging to detect more of our radio sources. The *HST* imaging can also be used to confirm that the CTIO imaging is sensitive to $I = 23.5$.

Table 6 lists the CTIO and *HST* I magnitudes of the ATHDF-S sources which lie in the WFPC2 deep and flanking fields. There are 35 radio sources within this region, and of these, 22 have CTIO counterparts. Five of the 13 sources without CTIO counterparts (i.e. I mag > 23.5) are identified in the WFPC2 imaging (F814W < 26.0). If the sample within the WFPC2 deep and flanking fields is representative of the full ATHDF-S radio sample, then 67% of our radio sources are detected to I mag = 23.5 (CTIO limit) and 79% to I mag $\sim$ 26.0 (WFPC2 limit). This is consistent with the HDF-N and small science aperture (SSA) 13 fields, where a sub-mJy radio source identification rate of 80% was achieved for a limit of I mag = 25.0 (Richards et al. 1999).

This implies that there is a sizable proportion of sub-mJy radio sources with very faint optical counterparts ($I_{AB} > 26$). We use the I mag limit to calculate the lower limit to the radio-to-optical ratio (see Section 5.2) of these sources. Table 7 lists the 1.4 GHz flux density and radio-to-optical ratio (R_I) limit for these eight sources. We find that all of these optically unidentified sources have relatively high radio-to-optical ratios ($R_I > 2.5$). Four sources have $R_I > 3$, which meets the criteria for radio-loud AGNs discussed in Section 5.2. Redshifts are required before we can firmly rule out star-formation processes as the source of the radio emission. However, we do note that these sources may be similar to the optically faint microjansky sources identified in radio observations of the HDF-N and SSA 13 fields (Richards et al. 1999).

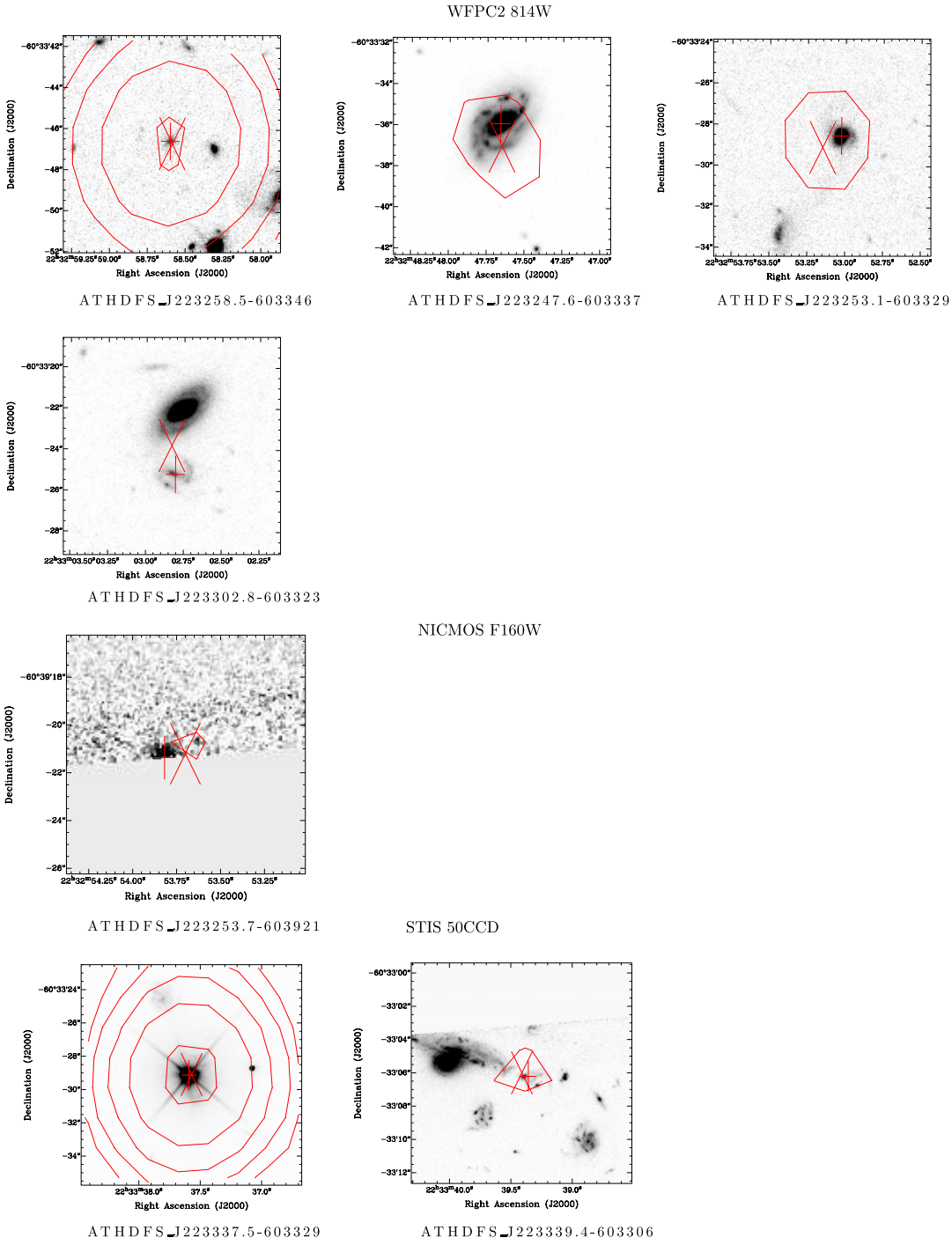

Figure 8. Gray-scale postage stamp images of the *HST* deep field counterparts to ATHDF-S radio sources. The crosses mark the radio position and the plus signs mark the optical positions. The contours are 1.4 GHz flux densities, set at 5, 10, 20, 50, 100, and 200σ.

(A color version of this figure is available in the online journal)

Because of their faintness, not much is known about optically faint microjansky sources, but Richards et al. (1999) propose several possibilities for the nature of these radio sources: (1) luminous dust-enshrouded starbursts at high redshifts of $z = 1$–3, (2) extremely high redshift AGNs ($z > 6$), or (3) luminous obscured AGNs at $z \gtrsim 2$. Submillimeter observations have shown that a significant fraction of these sources (at least 30%) are dusty starbursts at $1 < z < 3$ (Barger et al. 2000; Chapman et al. 2001, 2003). A large fraction ($\sim$50%) of the population also has detectable X-ray emission (Alexander et al. 2001), and the majority of these X-ray-detected sources have obscured AGN activity. A stacking analysis performed on the optically faint microjansky sources not detected by current X-ray observations found that their average X-ray properties are consistent with an object like Arp220 lying at $z \sim 1.5$ (Alexander et al. 2001). Recent high-resolution radio images

Table 5
Summary of *HST* Flanking Field Counterparts

ATHDF-S name	Flanking field ID	F606 magnitude	F606 rms error	F814 magnitude	F814 rms error	Morphological information
WFPC2 flanking observations						
ATHDF-S_J223207.9−603928	WdpVI	26.46	0.21	25.61	0.15	No info
ATHDF-S_J223253.7−603921	W9	...	...	21.12	0.01	Possible merging system
ATHDF-S_J223245.6−603857	W9	...	...	23.91	0.04	No info
ATHDF-S_J223248.2−603805	W9	...	...	20.90	0.01	Edge-on disk galaxy
ATHDF-S_J223254.5−603748	W9	...	...	18.44	0.00	Barred spiral
ATHDF-S_J223202.5−603714	WdpVI	25.86	0.11	24.17	0.04	Possible merging system
ATHDF-S_J223253.0−603539	W6	...	...	23.45	0.04	No info
ATHDF-S_J223245.3−603537	W6	...	...	24.04	0.06	No info
ATHDF-S_J223338.8−603523	W8	...	...	18.99	0.00	Early-type spiral
ATHDF-S_J223344.9−603515	W8	...	...	19.51	0.00	Spiral galaxy in merging system
ATHDF-S_J223350.5−603503	W8	...	...	26.24	0.19	No info
ATHDF-S_J223307.1−603448	W3	...	...	24.83	0.08	No info
ATHDF-S_J223243.3−603443	W2	...	...	19.32	0.00	Merging system
ATHDF-S_J223245.5−603419	W2	...	...	21.10	0.01	Possible merger
ATHDF-S_J223311.9−603417	W3	...	...	23.93	0.05	No info
ATHDF-S_J223306.0−603350	W3	...	...	17.25	0.00	Face-on spiral
ATHDF-S_J223243.4−603352	W2	...	...	19.87	0.00	Point-like, quasar
ATHDF-S_J223247.6−603337	W2	...	...	19.64	0.01	Spiral
ATHDF-S_J223337.5−603329	W8	...	...	17.70	0.00	Bright point source (STIS QSO)
ATHDF-S_J223339.4−603306	W8	...	...	24.81	0.10	No info
ATHDF-S_J223308.6−603251	W1	...	...	21.03	0.01	Spheroidal
ATHDF-S_J223317.7−603235	W4	...	...	20.83	0.01	Spheroidal
ATHDF-S_J223331.6−603222	W7	...	...	20.38	0.01	Merging system, triple nuclei
ATHDF-S_J223303.1−603132	W1	...	...	24.05	0.05	No info
NICMOS flanking observations						
ATHDF-S name	Flanking field ID	F111 magnitude	F111 rms error	F160 magnitude	F160 rms error	Morphological information
ATHDF-S_J223250.6−604336	N9	...	...	22.06	0.02	Possible merging system
ATHDF-S_J223337.5−604006	N8	...	...	19.66	0.00	Merging system
ATHDF-S_J223334.4−603804	N7	...	...	22.30	0.09	No info (at edge of image)
ATHDF-S_J223210.3−604433	dpJH	20.45	0.03	19.83	0.01	No info (at edge of image)
STIS flanking observations						
ATHDF-S name	Flanking field ID	50ccd magnitude	50ccd rms error			Morphological information
ATHDF-S_J223425.0−603452	S8	23.18	0.01			Disturbed, merging system
ATHDF-S_J223327.6−603414	S2	28.17	0.18			No info

suggest that optically faint microjansky sources are examples of dusty high redshift starbursts, and some of these seem to be composite sources with an embedded AGN (Muxlow et al. 2005).

3. SPECTROSCOPIC DATA

3.1. Spectroscopy in the Literature

The AAO undertook a public domain redshift survey of the HDF-S using the upgraded low dispersion survey spectrograph (LDSS++). The HDF-S LDSS++ targets were selected from deep Anglo-Australian Telescope (AAT) Prime Focus Imaging to $R < 24$ of a 9×3 arcmin field covering the main WFPC2 and STIS *HST* fields (Glazebrook et al. 2006). A total of 225 targets were observed simultaneously. The spectra obtained have 8 Å spectral resolution and cover the wavelength range from 5300 Å to 10700 Å. Four radio sources have high quality (two or more lines) LDSS++ spectra, and we summarize the LDSS++ counterparts in Table 8. The spectra were examined and typed using the same criteria and nomenclature as the 2dF spectroscopy.

Spectroscopy was also obtained at the Very Large Telescope (VLT) using the FORS2 spectrograph in the multi-object spectroscopy (MOS) mode. A total of 194 galaxies in the main HDF-S and flanking fields were targeted during 2000 and 2002. Reliable redshifts, determined from multiple spectral features or the [O II] 3727 Å doublet, were obtained for 97 targets (Sawicki & Mallén-Ornelas 2003). Approximately half of all galaxies brighter than F814W(AB) = 24 in the HDF-S proper were observed, and redshifts were obtained for 76%. We cross-matched the ATHDF-S radio sources against the Sawicki & Mallén-Ornelas (2003) redshift catalog. A total of five counterparts were found and Table 9 summarizes the results.

3.2. 2dF Optical Spectroscopy

The public domain spectroscopic follow-up of galaxies in the HDF-S and the surrounding region has yielded about 400 redshifts (Vanzella et al. 2002, Sawicki & Mallén-Ornelas 2003, Glazebrook et al. 2006). Only six of our radio sources have spectroscopic redshifts from the literature, however. The main factor limiting the spectroscopic completeness is that these redshift surveys were concentrated on the central WFPC2 field and the surrounding *HST* flanking fields, whereas our radio sources are from a region 40 arcmin in diameter. Hence, we undertook wide-field spectroscopic observations.

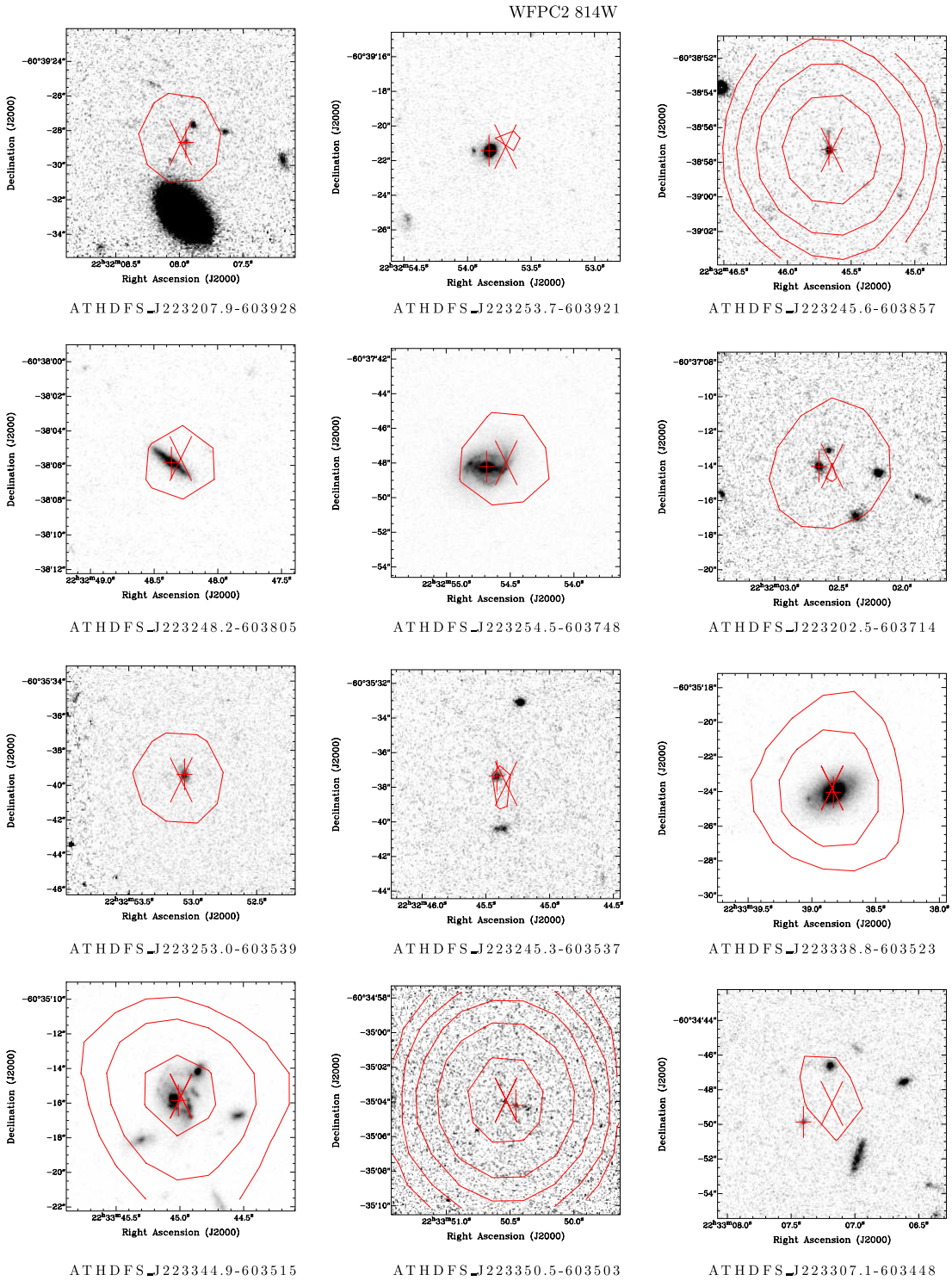

Figure 9. Gray-scale postage stamp images of the *HST* WFPC2 flanking field counterparts to ATHDF-S radio sources. The crosses mark the radio position and the plus signs mark the optical positions. The contours are 1.4 GHz flux densities, set at 5, 10, 20, 50, 100, and 200σ.

(A color version of this figure is available in the online journal)

We obtained spectra of the ATHDF-S radio sources over two service nights in 2001 July and 2003 October using the multi-fiber 2dF instrument of the AAT. The 2dF allows the simultaneous acquisition of up to 400 spectra over a 2 deg diameter region of sky. We employed the 2dFGRS (Colless et al. 2001) observing strategy, which is to use a 300 line mm^{-1} grating at a central wavelength of 5800 Å. This yielded low-resolution (9 Å) spectra over the wavelength range 3800–8000 Å. Our data consisted of six consecutive 20 min exposures, giving a total of 2 h on source.

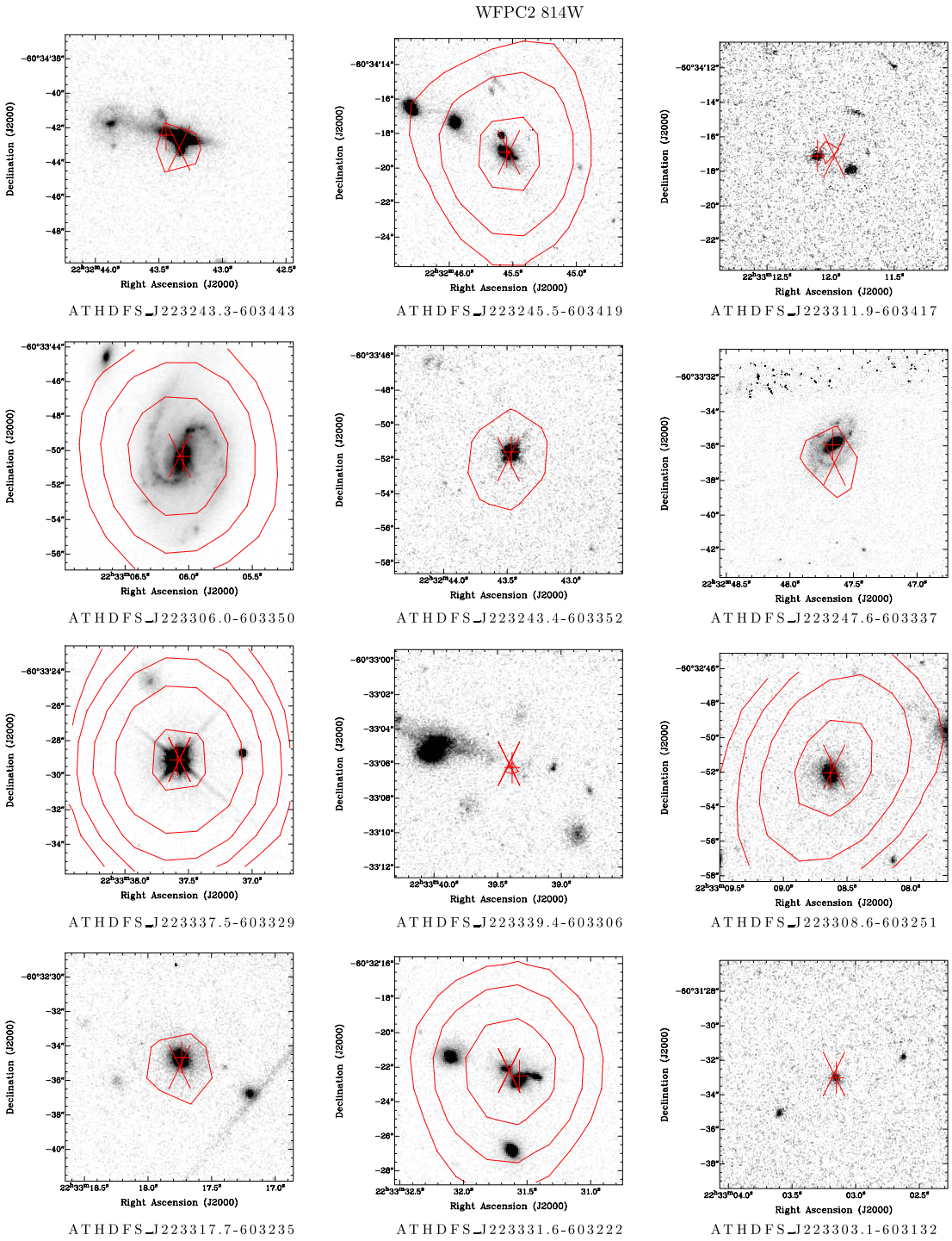

Figure 10. More gray-scale postage stamp images of the *HST* WFPC2 flanking field counterparts to ATHDF-S radio sources. The crosses mark the radio position and the plus signs mark the optical positions. The contours are 1.4 GHz flux densities, set at 5, 10, 20, 50, 100, and 200σ.

(A color version of this figure is available in the online journal)

The spectra were reduced using the *2dfdr* reduction package, developed by the AAO specifically for 2dF spectra data. We were unable to place a fiber on all targets due to crowding, so higher priority was given to our radio sources with bright (B $<$ 23) counterparts. A total of 268 sources from the 1.4 GHz ATHDF-S catalog were targeted. Redshifts were determined by visually inspecting the spectra. Each spectrum was assigned an index, Q, that signifies the quality of the redshift determination. A value of $Q = 3$ indicates that three or more lines were identified, so the redshift is very well determined. $Q = 2,1$, or 0, indicates two, one or no lines identified respectively. Redshifts were obtained for 98 out of the 268 targeted sources. In Figure 12, we plot B magnitude against 1.4 GHz flux density for the ATHDF-S radio sources. From this we can see that the

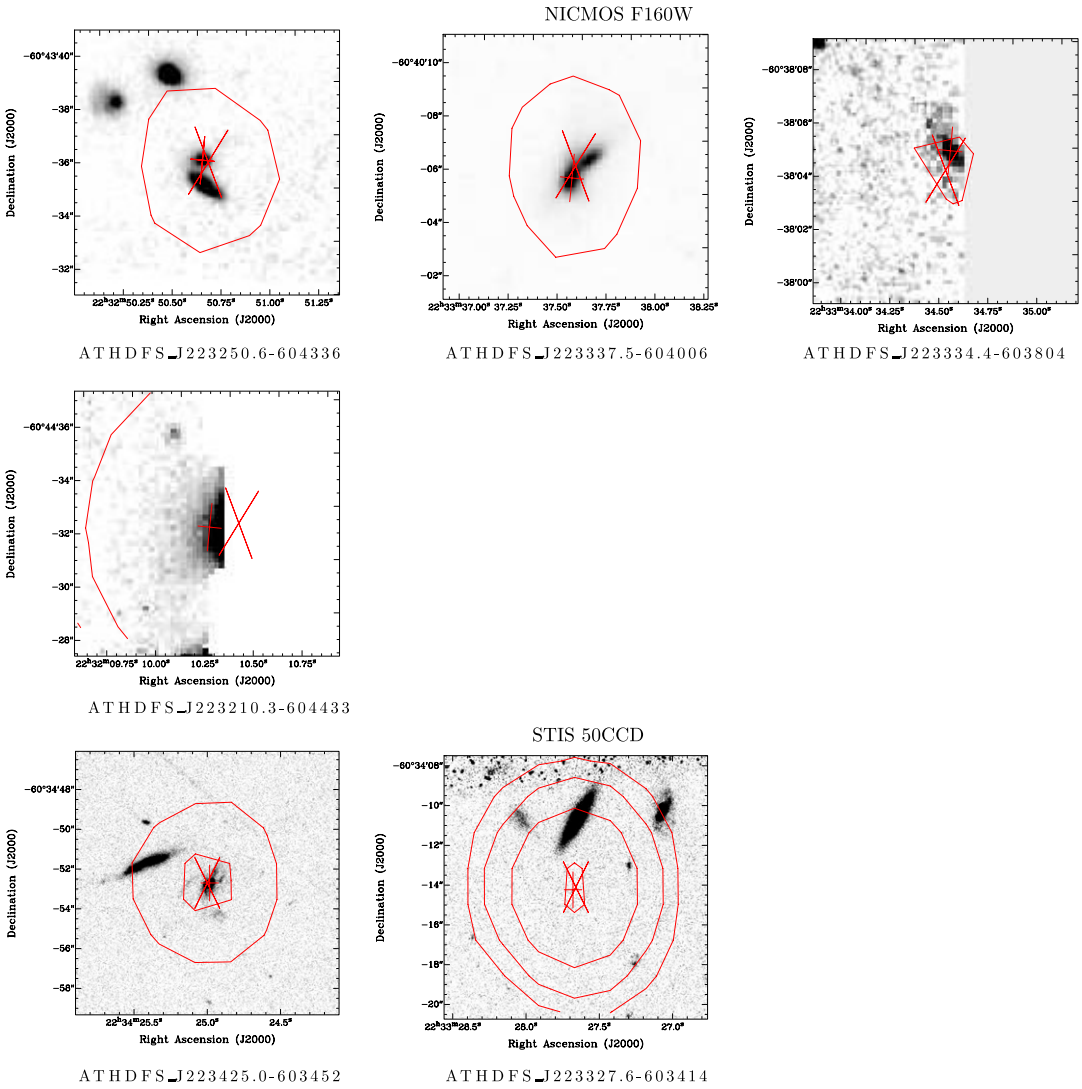

Figure 11. Gray-scale postage stamp images of the *HST* NICMOS and STIS flanking field counterparts to ATHDF-S radio sources. The crosses mark the radio position and the plus signs mark the optical positions. The contours are 1.4 GHz flux densities, set at 5, 10, 20, 50, 100, and 200σ.

(A color version of this figure is available in the online journal)

2dF success rate is almost 100% for all targeted sources brighter than about $B = 22$. Redshifts are much harder to obtain for the fainter sources. In the $B > 23$ cases, the spectra are low S/N and the redshift determination is only possible by the detection of bright emission lines.

The spectra were also used to classify our radio sources. We divided the spectra into five broad classes:

(i) galaxies with absorption line spectra (22, 22%),
(ii) star-forming galaxies (36, 37%),
(iii) Seyfert galaxies (6, 6%),
(iv) broadline AGNs (7, 7%),
(v) unclassified objects (27, 28%).

The unclassified objects have at least one identifiable line in their spectrum, but insufficient S/N or not enough observed lines to make a classification possible.

The Seyferts were determined by [O III] 5007/Hβ and [N II]6583/Hα diagnostic line ratios. Although the 2dF spectrograph is fiber fed, these line pairs are close in wavelength and thus poor flux calibration will not affect these line ratios significantly. The line ratios of all our star-forming and Seyfert objects are plotted in Figure 13 along with the Kewley et al. (2001) classification line. The six Seyferts lie above and to the right of the maximum starburst line.

In Table 10 we present a summary of the 2dF spectroscopy of the ATHDF-S sources. Information is provided for the sources with 2dF redshifts. A description of Table 10 is as follows:

Column 1: ATHDF-S source name.
Column 2: 2dF spectroscopic redshift.
Column 3: quality of 2dF spectroscopy, as described above.
Column 4: spectral classification, as described above. "abs" are galaxies with absorption lines, "sf" are star-forming galaxies, "sy" indicates Seyferts, "BL" marks broadline AGNs, and "unc" means unclassified.
Column 5: Hβ line flux, in CCD counts.
Column 6: O III[5007] line flux, in CCD counts.
Column 7: Hα line flux, in CCD counts.
Column 8: N II[6584] line flux, in CCD counts.
Column 9: comments on spectra, including which lines are observed.

Table 6
The *I* Magnitudes of ATHDF-S Sources in the *HST* WFPC2 Deep and Flanking Fields

ATHDF-S name	CTIO I magnitude	*HST* F812W magnitude	$S_{1.4\,\mathrm{GHz}}$ (mJy)
ATHDF-S_J223207.9−603928	...	25.61	0.098
ATHDF-S_J223253.8−603921	20.68	21.12	0.052
ATHDF-S_J223245.6−603857	23.39	23.91	0.843
ATHDF-S_J223248.2−603805	20.49	20.90	0.076
ATHDF-S_J223254.5−603748	17.91	18.44	0.092
ATHDF-S_J223202.5−603714	23.60	24.17	0.148
ATHDF-S_J223253.0−603539	23.19	23.45	0.090
ATHDF-S_J223245.3−603537	23.77	24.04	0.051
ATHDF-S_J223338.8−603523	18.61	18.99	0.185
ATHDF-S_J223344.9−603515	18.69	19.51	0.344
ATHDF-S_J223350.5−603503	23.08	26.24	1.252
ATHDF-S_J223307.1−603448	...	24.83	0.103
ATHDF-S_J223243.3−603443	18.87	19.32	0.063
ATHDF-S_J223245.5−603419	20.33	21.10	0.265
ATHDF-S_J223311.9−603417	23.09	23.93	0.059
ATHDF-S_J223306.0−603350	16.58	17.25	0.452
ATHDF-S_J223258.6−603346	...	25.12	1.010
ATHDF-S_J223243.4−603352	19.45	19.87	0.098
ATHDF-S_J223247.6−603337	19.16	19.55	0.075
ATHDF-S_J223337.5−603329	16.51	17.70	1.126
ATHDF-S_J223253.1−603329	22.29	22.56	0.113
ATHDF-S_J223303−603324	22.31	22.79	0.051
ATHDF-S_J223339.4−603306	...	24.81	0.058
ATHDF-S_J223308.6−603251	20.45	21.03	0.821
ATHDF-S_J223317.7−603235	19.57	20.83	0.070
ATHDF-S_J223331.6−603222	19.90	20.38	0.395
ATHDF-S_J223303.1−603132	...	24.05	0.052

Notes. The eight sources not detected by CTIO and *HST* are listed separately in Table 7.

Table 7
ATHDF-S Sources in the *HST* WFPC2 Deep and Flanking Fields which Remain Undetected to $I \sim 26.0$

ATHDF-S name	$S_{1.4\,\mathrm{GHz}}$ (mJy)	Radio-to-optical ratio R_I
ATHDF-S_J223258.7−603903	0.058	>2.60
ATHDF-S_J223205.9−603857	0.254	>3.24
ATHDF-S_J223327.6−603414	0.456	>3.50
ATHDF-S_J223327.9−603304A	0.221	>3.18
ATHDF-S_J223327.9−603304B	0.059	>2.61
ATHDF-S_J223323.2−603249	0.457	>3.50
ATHDF-S_J223335.3−603234	0.054	>2.47
ATHDF-S_J223302.1−603213	0.063	>2.64

4. PHOTOMETRIC REDSHIFTS

The majority of our radio sources do not have spectral data, but CTIO imaging provides up to five-band photometry of 67% of the radio sources with which to calculate photometric redshifts. Photometric redshifts were determined using the galaxy template technique by two independent groups: Teplitz et al. (2001) and ourselves. Teplitz et al. (2001) used a template set which consisted of Coleman et al. (1980) spectra augmented with a single bluer synthetic starburst (Bruzual & Charlot 1993). They calculated photometric redshifts for objects with a clear detection ($>3\sigma$) in *BVR* and either *u* or *I*. We adopted the template set of Coleman et al. (1980) spectra plus two starburst galaxy spectra. The two new starburst galaxy spectra were formed by adopting starbursts SB1 and SB2 of Kinney et al. (1996), which have different intrinsic color excess, and extrapolating to ultraviolet and near-IR wavelengths using the recipe from Fernández-Soto et al. (1999).

Teplitz et al. (2001) performed a Monte Carlo simulation to estimate the accuracy of their photometric redshifts. Model galaxy spectra (Bruzual & Charlot 1993) of varying metallicity and age were redshifted and random photometric error added. The redshift error from applying the photometric redshift method to the simulated spectra is typically 15–20% for $z < 1$ (Teplitz et al. 2001). For galaxies with $z > 1$ the typical residuals in the redshift error are $\Delta z > 0.35$. Also, the failures ($\Delta z > 0.33$) for $z < 1$ simulated galaxies are less than 10%, compared with greater than 40% for $z > 1.33$ objects. The failures in the Teplitz et al. (2001) photometric redshift catalog are likely to

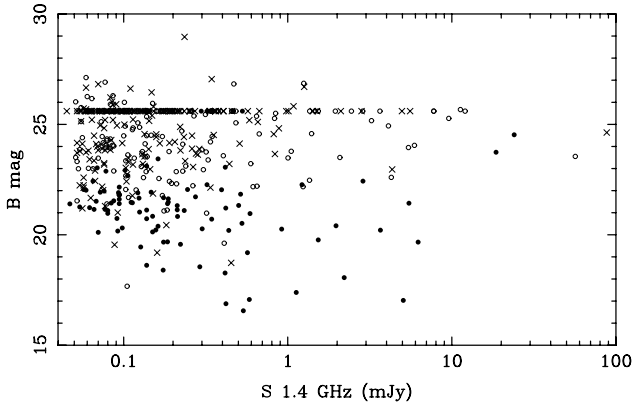

Figure 12. *B*-band magnitude versus 1.4 GHz flux density for all ATHDF-S radio sources. The solid circles are sources with redshifts successfully obtained from 2dF. The empty circles are 2dF targeted sources, but no redshift was determined. The crosses mark sources which were not targeted in the 2dF observations. Radio sources without optical counterparts are placed at $B = 25.6$, the nominal *B*-band limit of the CTIO observations. We note that in two cases with $B < 20$ no redshift was recorded. The first case is ATHDF-S_J223222.4−602532, which is near a star, so the *B* magnitude of 17.67 is probably overestimated. We suspect that the fiber was incorrectly placed for the second case (ATHDF-S_J223414.7−604753).

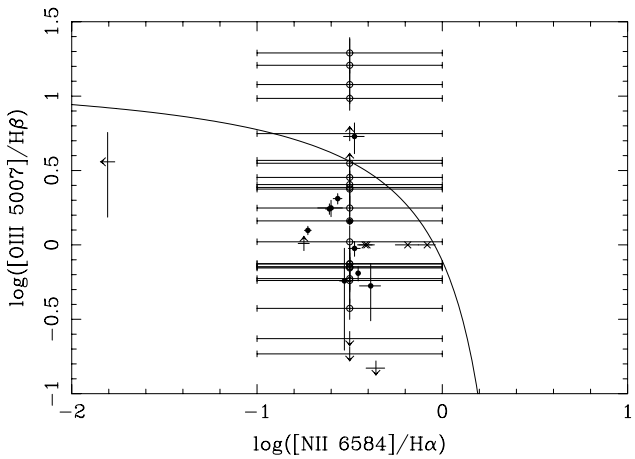

Figure 13. Diagnostic line ratio [N II]6583/Hα against [O III]5007/Hβ for the 42 narrowline emitting galaxies in our 2dF sample. The solid circles indicate sources where all four lines are detected. The open circles mark high redshift galaxies where the Hα and N II lines are out of the wavelength coverage. For these sources the uncertainty in [N II]6583/Hα is marked by large error bars. The crosses mark sources with no detectable Hβ or [O III]5007 emission. The arrows indicate upper and lower limits. The solid curve is the theoretical maximum starburst line from Kewley et al. (2001). Star-forming galaxies lie below this line, while AGNs are found above this line.

Table 8
Summary of LDSS++ Spectra (Glazebrook et al. 2006) of ATHDF-S Radio Sources

ATHDF-S name	LDSS++ number	Redshift	Spectral type	Comments
ATHDF-S_J223241.4−603025	216	0.4250	abs	O II, Balmer-, HK, Hβ+
ATHDF-S_J223247.6−603337	196	0.5803	abs	O II, HK, Hδ-, G, Hγ-
ATHDF-S_J223306.0−603350	133	0.1733	sf	Hβ+, O III+, Mgb, 5268, Hα+, N II+, S II+
ATHDF-S_J223245.5−603419	204	0.4606	sf	Hβ+, O III(4959+5007)+

Table 9
Summary of FORS2 Spectra (Sawicki & Mallén-Ornelas 2003) of ATHDF-S Radio Sources

ATHDF-S name	Sawicki & Mallén-Ornelas (2003) ID	Redshift	Comments
ATHDF-S_J223254.5−603748	90549	0.2668	
ATHDF-S_J223243.3−603443	20277	0.4233	
ATHDF-S_J223245.5−603419	20462	0.4608	
ATHDF-S_J223247.6−603337	672	0.5807	
ATHDF-S_J223302.8−603323	894	0.4642	

be more numerous, since real data contain a larger variety of galaxies, such as AGNs. Nevertheless, one can conclude that their photometric redshifts are quite reliable to $z = 1$. The reason for the failure at $z > 1$ is the limitations of the CTIO filter set. The most obvious spectral features for template fitting are the 4000 Å and 912 Å breaks, which fall out of the *uBVRI* passbands. The 4000 Å is shifted to near-IR for $z > 1$, while the 912 Å is out of the *u* passband until $z \sim 2.5$. The CTIO photometric redshifts are listed in Table 11.

We expect our photometric redshifts to have similar accuracy, since similar data and techniques are used. A photometric redshift was estimated for the 307 1.4 GHz radio sources with a CTIO counterpart from the CTIO imaging. The photometric redshifts are restricted to $0 < z < 1$, as this is the redshift space effectively probed by the *uBVRI* filter set. Photometric redshifts of $z = 0$ and $z = 1$ were rejected since the photometric redshift code obviously did not find a fit within the desired range. This occurred for 43 of the sources, so in total we derive 264 photometric redshifts. We list these in Table 11.

To investigate the accuracy of our photometric redshifts we compared them with the spectroscopic ones obtained on 2dF. Of the 98 objects with 2dF redshifts, 85 have photometric redshifts. We show a comparison of the 2dF spectroscopic versus photometric redshifts in the left panel of Figure 14. We find that only six ATHDF-S sources have estimated photometric redshifts which are failures ($\delta z/(1+z_{\rm spec}) > 0.2$), indicating a high photometric redshift success rate of 79/85 (93%). Four of these sources are broadline emitting quasars which are not well represented by our galaxy templates. The 79 successful photometric redshifts have a median residual $\delta z/(1+z_{\rm spec})$ of 0.008 ± 0.064. In comparison, there are photometric redshifts from Teplitz et al. (2001) for 87 of the sources with 2dF redshifts. A comparison of Teplitz et al. (2001) and 2dF redshifts is shown in the right panel of Figure 14. The success rate ($\delta z/(1+z_{\rm spec}) < 0.2$) of the Teplitz et al. (2001) photometric redshifts is 72/87 (83%). We note that there are eight sources with a spectroscopic redshift $z < 1$ which are erroneously given photometric redshifts $z > 1$ by Teplitz et al. (2001). Also, even though Teplitz et al. (2001) allow photometric redshifts greater than $z = 1$, they successfully estimate the redshift of only 1/6 of the broadline emitting objects at $z > 1$. We therefore deem our photometric redshifts to be more reliable than Teplitz et al. (2001) and use only our photometric redshifts in further analysis.

The photometric redshifts are accurate for the 2dF sample. However, is this likely to be true for the full ATHDF-S sample? The sources with 2dF redshifts are the optically brightest of our sources (see Figure 12), so the previous comparison between photometric and spectroscopic redshifts is not from a random selection of the full ATHDF-S sample. To estimate the contamination in the photometric redshifts we can combine the results from Teplitz et al. (2001) with ours. Figure 15 shows the comparison of the 209 sources which also have photometric redshifts from Teplitz et al. (2001). In the cases where Teplitz et al. (2001) $z < 1$, which is 185/209 (89%), there is good agreement, and the median $\delta z/(1+z_{\rm phot})$ is -0.046 ± 0.097. The two photometric redshift samples are independent fits, yet they agree ($\delta z/(1+z_{\rm phot}) < 0.2$) for ~87% of the sources with Teplitz et al. (2001) redshifts. By design, our photometric redshifts will be wrong for sources that actually lie at $z > 1$, but from Figure 15 we see that sources which are possibly at $z > 1$ (from Teplitz et al. 2001) have a flat distribution in our photometric redshifts, and hence are not biased to a particular redshift. It is not clear whether the Teplitz et al. (2001) redshifts are overestimated or our redshifts underestimated for the discordant cases. However, it is likely that our results are correct for a significant portion of these discordant cases since the Teplitz et al. (2001) results have a 40% failure rate for $z > 1$.

The photometric redshifts of our ATHDF-S radio sources are listed in Table 11. A description of the table is as follows:

Column 1: ATHDF-S source name.
Column 2: Teplitz et al. (2001) photometric redshift.
Column 3: photometric redshift from this work.
Column 4: best-fit spectral template, as described above.

5. DISCUSSION

5.1. Optical Properties of the Sub-mJy Sample

The magnitude distributions of our matched radio sources, at all five CTIO optical bands, are shown in Figure 16. The *R* magnitude distribution shows that the number of sources declines between $R = 22$ and $R = 24$, and there are similar decreases in the other passbands. We argue that this is a property of the CTIO-identified ATHDF-S radio sources, rather than being caused by incompleteness in the optical imaging, since the drop-off in number occurs well above the limiting magnitude of

Table 10
Summary of 2dF Spectral Properties for ATHDF-S Sources with 2dF Redshifts

ATHDF-S name	2dF redshift	2dF quality	Spectral type	Hβ line flux	O III [5007] line flux	Hα line flux	N II [6584] line flux	Comments
ATHDFS_J223356.6-601949	0.2856	3	abs	...	...	...	...	OII, HK, G, Mg
ATHDFS_J223358.9-602258	2.519	3	BL	...	...	...	...	La, OIV], CIV and CIII]
ATHDFS_J223134.5-602457	0.5636	2	unc	...	...	...	...	OII, HK
ATHDFS_J223141.1-602506	0.2485	3	sf	1180 ± 230	680 ± 210	...	...	OII, HK, Hb, OIII
ATHDFS_J223136.9-602610	0.5189	2	unc	...	...	...	...	OII, H, K
ATHDFS_J223335.3-602615	0.1726	3	sf	<70	<70	3860 ± 230	3200 ± 280	OII, HK, Ha, N2
ATHDFS_J223400.9-602633	0.4314	3	abs	...	...	...	...	H, K, G, Mg
ATHDFS_J223418.3-602715	0.3034	1	unc	...	...	...	...	OII
ATHDFS_J223311.5-602725	0.1084	3	sf	<130	<130	9050 ± 470	3470 ± 260	OII, HK, G, weak Hb, weak OIII, Ha, N2, S2
ATHDFS_J223443.9-602739B	0.4415	2	abs	...	...	...	...	HK, G
ATHDFS_J223330.5-602849	0.4149	3	sf	1730 ± 130	6120 ± 280	...	...	OII, Hb, OIII
ATHDFS_J223515.2-602856	0.4424	3	sf	350 ± 90	890 ± 170	...	...	OII, HK, Hb, OIII
ATHDFS_J223431.7-602859	0.4275	3	sf	640 ± 130	<150	-	...	OII, H, K, Hb
ATHDFS_J223415.3-602925	0.1679	3	sf	<100	<100	4870 ± 330	3170 ± 400	OII, HK, G, Hb, OIII, Ha, N2, S2
ATHDFS_J223108.1-602946	0.5646	1	unc	...	...	...	...	OII
ATHDFS_J223534.2-602948	0.1752	3	sf	<50	<50	5050 ± 260	1980 ± 160	OII, Mg, Na, Ha, N2
ATHDFS_J223440.4-603017	0.3251	3	abs	...	...	...	...	HK, Hb abs, G, Mg,
ATHDFS_J223120.1-603025	0.4239	2	unc	...	...	...	...	OII, H
ATHDFS_J223304.8-603031	0.4282	3	unc	...	...	...	...	OII, Hb, OIII
ATHDFS_J223504.6-603109	0.0587	3	sf	6250 ± 460	12800 ± 400	35700 ± 800	9730 ± 480	OII, HK, G, Hb, OIII, Ha, N2, S2
ATHDFS_J223519.4-603157A	0.4081	3	sf	2030 ± 220	1510 ± 230	...	...	OII, Hb, OIII
ATHDFS_J223519.4-603157B	0.4067	3	sf	800 ± 80	570 ± 70	...	...	OII, HB, OIII
ATHDFS_J223343.5-603211	0.5302	3	sf	370 ± 110	878 ± 150	...	...	OII, HK, Hb, OIII
ATHDFS_J223504.4-603221	0.4265	1	unc	...	...	...	...	OIII
ATHDFS_J223331.6-603222	0.4652	3	sf	650 ± 120	1150 ± 100	...	...	OII, Hb, OIII
ATHDFS_J223509.4-603235	0.1200	3	abs	...	...	...	...	H, K, Hb, OIII, Mg, Na
ATHDFS_J223142.5-603238	0.3445	2	abs	...	...	...	...	H, K, Mg
ATHDFS_J223337.5-603329	2.238	3	BL	...	...	...	...	STIS QSO z = 2.238
ATHDFS_J223513.7-603333	0.4070	2	sf	810 ± 150	<150	...	...	OII, HB
ATHDFS_J223225.0-603338	0.2998	2	sf	...	1210 ± 120	-	...	OII, OIII
ATHDFS_J223243.4-603352	1.566	3	BL	...	...	...	...	CIV, CIII] and MgII
ATHDFS_J223401.0-603424	0.2832	2	abs	...	...	...	...	HK, Mg, G
ATHDFS_J223442.8-603433	0.0668	3	sf	680 ± 390	2460 ± 110	1920 ± 140	<30	OII, Hb, OIII, Ha
ATHDFS_J223212.3-603448	0.1823	2	unc	...	...	...	...	OII, OIII
ATHDFS_J223438.6-603450	0.3354	3	abs	...	...	...	...	HK, G, Hb abs, Mg
ATHDFS_J223541.5-603454	0.6142	1	unc	...	...	...	...	OII
ATHDFS_J223344.9-603515	0.5273	3	sf	2510 ± 230	940 ± 120	...	...	OII, Hb, OIII
ATHDFS_J223208.3-603519	0.2841	3	sy	600 ± 160	11700 ± 400	...	...	OII, HK, OIII
ATHDFS_J223338.8-603523	0.2250	3	abs	...	...	...	...	H, K, G, OIII
ATHDFS_J223046.1-603525	0.3002	3	sf	2200 ± 210	6250 ± 260	...	...	OII, Hb, OIII
ATHDFS_J223232.4-603542A	0.4338	2	abs	...	...	...	...	HK, G
ATHDFS_J223232.4-603542B	0.4338	2	abs	...	...	...	...	HK, G
ATHDFS_J223525.7-603544	0.0586	3	sf	3320 ± 380	5880 ± 310	19700 ± 700	4940 ± 730	OII, Hb, OIII, Ha, N2, S2
ATHDFS_J223104.8-603549	0.5693	1	unc	...	...	...	...	OII
ATHDFS_J223421.8-603603	0.3499	3	sf	3840 ± 250	2280 ± 340	-	...	OII, Hb, OIII
ATHDFS_J223158.5-603614	0.4213	2	unc	...	...	...	...	OII, K
ATHDFS_J223451.7-603632	0.3291	3	sf	900 ± 110	640 ± 190	...	...	OII, H, K, Hb, OIII
ATHDFS_J223406.7-603637	0.0991	3	sf	3750 ± 300	3550 ± 290	21200 ± 400	7120 ± 500	OII, HK, Hb, OIII, Na, Ha, N2, S2
ATHDFS_J223400.2-603653	0.0992	3	sf	7070 ± 480	4560 ± 410	64600 ± 820	22700 ± 560	OII, HK, Hb, OIII, Na, Ha, N2, S2
ATHDFS_J223417.1-603724	0.2403	3	abs	...	...	...	...	OII, HK, G, Mg, some OIII
ATHDFS_J223437.7-603726	0.4137	3	sf	4420 ± 160	3310 ± 310	...	...	OII, Hb, OIII
ATHDFS_J223254.5-603748	0.1798	3	sy	840 ± 190	4500 ± 260	5420 ± 210	1820 ± 220	OII, H, K, Hb, OIII, Ha, N2
ATHDFS_J223418.6-603808	0.4279	3	sy	2010 ± 140	19400 ± 200	-	...	OII, Hb, OIII
ATHDFS_J223450.4-603844	0.4180	2	abs	...	...	...	...	K, G
ATHDFS_J223153.7-603853	0.7500	1	unc	...	...	...	...	OII
ATHDFS_J223144.4-603858	0.3102	3	abs	...	...	...	...	H, K, G, Hb, Mg
ATHDFS_J223123.1-603903	0.2782	1	unc	...	...	...	...	OII
ATHDFS_J223222.7-603924	0.4215	2	unc	...	...	...	...	OII, K, G
ATHDFS_J223220.6-603931	0.2825	3	abs	...	...	...	...	HK, G, Na, Mg
ATHDFS_J223337.5-604006	0.425	3	sf	530 ± 110	1290 ± 140	...	...	OII, Hb, OIII
ATHDFS_J223448.3-604042	0.1463	3	sf	<4000	4090 ± 280	18600 ± 500	3330 ± 210	OII, HK, OIII, Ha
ATHDFS_J223255.4-604151	1.233	2	BL	...	...	...	...	MgII, CIII]
ATHDFS_J223359.8-604155	0.0582	3	abs	...	...	...	...	OII, H, K, G, Mg, Ha, N2
ATHDFS_J223437.2-604214	0.4645	2	unc	...	...	...	...	OII, HK
ATHDFS_J223338.8-604216	0.3113	3	sf	5690 ± 200	8250 ± 350	...	-	OII, HK, Hb, OIII

Table 10
(Continued)

ATHDF-S name	2dF redshift	2dF quality	Spectral type	Hβ line flux	O III [5007] line flux	Hα line flux	N II [6584] line flux	Comments
ATHDFS_J223312.4-604227	0.5244	1	unc	...	...	...	...	OII
ATHDFS_J223207.9-604305	0.7570	2	unc	...	...	...	...	OII, HK
ATHDFS_J223240.2-604306	0.2982	2	sy	<2000	11200 ± 600	...	-	OII, Hb, OIII, HK
ATHDFS_J223430.8-604310	0.3394	2	sf	<200	740 ± 180	-	...	OII, OIII
ATHDFS_J223440.4-604309	0.3124	2	unc	...	...	...	...	OII, H, K
ATHDFS_J223522.2-604326	0.1772	3	sf	4830 ± 360	2560 ± 1050	5600 ± 490	2300 ± 220	OII, Hb, Ha, N2, HK
ATHDFS_J223126.2-604337	0.0864	3	sf	5500 ± 350	9600 ± 480	27100 ± 500	6660 ± 300	OII, OIII, Hb, Ha, N2, S2
ATHDFS_J223313.9-604359	0.1758	3	sf	1010 ± 130	<150	7530 ± 270	3300 ± 360	OII, H, K, G, Hb, Ha, N2, S2
ATHDFS_J223319.1-604428	0.6465	2	BL	...	...	...	...	
ATHDFS_J223121.4-604448	0.6023	1	unc	...	...	...	...	OII
ATHDFS_J223443.3-604452	3.1	2	BL	...	...	...	...	
ATHDFS_J223342.9-604524	0.2454	3	sy	480 ± 240	7740 ± 350	...	-	OII, OIII, HK, weak Hb
ATHDFS_J223536.8-604632	0.1775	3	sf	3790 ± 480	2170 ± 1400	25900 ± 500	7670 ± 420	Hb, Ha, low OIII, N2, OII
ATHDFS_J223527.8-604639A	0.4649	2	abs	...	...	...	...	H, K
ATHDFS_J223333.2-604642	0.1393	3	abs	...	...	...	...	abs HK, Na
ATHDFS_J223228.5-604642	0.6370	1	unc	...	...	...	...	H, K, G
ATHDFS_J223417.5-604749	0.2015	3	sf	600 ± 130	420 ± 150	-	...	OII, H, K, Hb, OIII, Ha, N2
ATHDFS_J223217.6-604751	0.7103	1	unc	...	...	...	...	OII
ATHDFS_J223243.0-604758	0.5810	2	unc	...	...	...	...	Hb, OIII but lines in red skylines
ATHDFS_J223452.0-604834	0.2461	2	unc	...	...	...	...	OII, no Hb or OIII
ATHDFS_J223337.8-604833	0.5121	1	unc	...	...	...	...	OII
ATHDFS_J223413.1-604909	0.2653	3	abs	...	...	...	...	OII, HK, Hb
ATHDFS_J223226.9-605029	0.4015	1	unc	...	...	...	...	OII
ATHDFS_J223139.6-605039	0.2834	3	abs	...	...	...	...	H, K, G, Hb, Mg
ATHDFS_J223352.5-605210	0.2540	1	unc	...	...	...	...	OII
ATHDFS_J223454.9-605211	0.0557	3	sf	47500 ± 1100	68300 ± 800	317400 ± 2200	100600 ± 1700	OII, Hb, OIII, Ha, N2, S2
ATHDFS_J223145.4-605311	0.3140	3	abs	...	...	...	...	strong HK, Hb abs, Mg, Na
ATHDFS_J223151.1-605328	0.3114	3	sy	1630 ± 420	19500 ± 400	-	...	OII, OIII, Hb, HK, Na
ATHDFS_J223204.8-605414	0.2817	3	sf	1010 ± 200	1060 ± 210	...	...	OII, H, K, Hb, OIII
ATHDFS_J223214.8-605430	1.073	2	BL	...	...	...	...	MgII, OII and CII
ATHDFS_J223316.9-605533	0.0553	3	abs	...	...	...	...	strong abs HK, Hb, Mg, Na
ATHDFS_J223314.6-605543	0.0563	3	sf	3170 ± 140	3970 ± 190	20300 ± 500	3820 ± 130	OII, H, K, Hb, OIII, Ha, N2, S2
ATHDFS_J223303.6-605751	0.2202	2	unc	...	...	...	...	OII, no Hb or OIII

(This table is also available in a machine-readable form in the online journal)

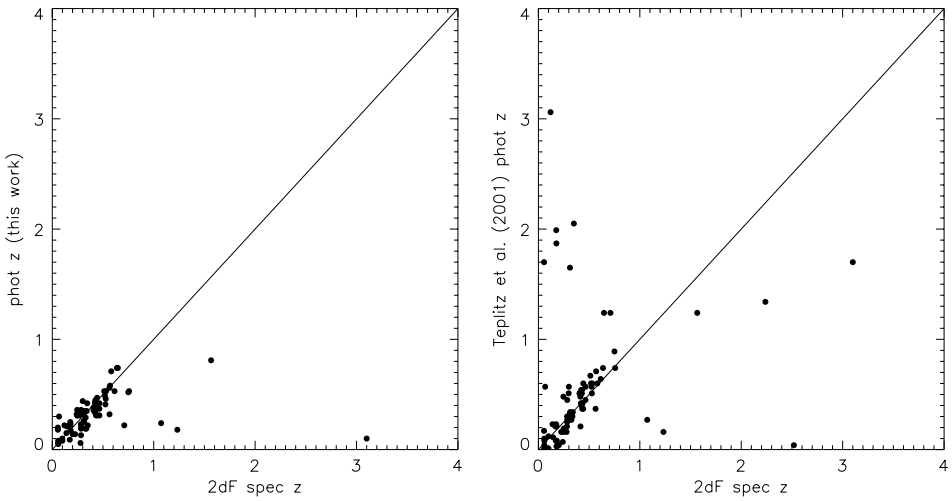

Figure 14. Left: comparison of 2dF spectroscopic and our photometric redshifts for the 85 ATHDF-S sources that have both. Right: comparison of 2dF spectroscopic and Teplitz et al. (2001) photometric redshifts for the 88 ATHDF-S sources that have both.

the optical data. The mean magnitude of the optical counterparts to our radio sources is 22.7, 23.0, 22.2, 21.3, and 20.4 for the U-, B-, V-, R-, and I-bands, respectively, whereas the limiting magnitude of the CTIO images are 24.0, 25.6, 25.0, 25.0, and 23.5 for the same passbands.

In Figure 17, we plot the I-band magnitude of the sample against 1.4 GHz flux density. The lower flux density sources seem to have fewer bright (I mag < 19) optical counterparts. The median I magnitude for sources with $S_{1.4\,\mathrm{GHz}} > 0.5$ mJy is 0.8 mag brighter than the median I magnitude of the faintest

Table 11
Photometric Redshifts of ATHDF-S Radio Sources

ATHDF-S name	Teplitz et al. (2001) redshift	Redshift (this work)	Spectral type
ATHDFS_J223316.9-605533	0.17	0.20	Sbc
ATHDFS_J223353.9-605452	0.98	0.75	Scd
ATHDFS_J223214.8-605430	0.27	0.24	Scd
ATHDFS_J223448.4-605417	0.71	0.80	Scd
ATHDFS_J223204.8-605414	0.21	0.33	Scd
ATHDFS_J223230.3-605352	0.82	0.85	Sbc
ATHDFS_J223151.1-605328	0.32	0.25	E/S0
ATHDFS_J223145.4-605311	0.32	0.25	E/S0
ATHDFS_J223453.4-605259	0.74	0.74	E/S0
ATHDFS_J223203.0-605242B	0.34	0.27	E/S0
ATHDFS_J223458.6-605225	0.71	0.71	E/S0
ATHDFS_J223345.4-605227	1.44	0.48	Irr
ATHDFS_J223454.9-605211	1.70	0.18	Scd
ATHDFS_J223241.8-605209	0.10	0.11	E/S0
ATHDFS_J223223.3-605137	0.51	0.37	E/S0
ATHDFS_J223323.8-605141	0.51	0.68	Scd
ATHDFS_J223420.1-605138	0.82	0.84	Sbc
ATHDFS_J223427.0-605132	0.51	0.38	Scd
ATHDFS_J223238.8-605113	0.78	0.88	Scd
ATHDFS_J223139.6-605039	0.25	0.19	E/S0
ATHDFS_J223142.8-605024	0.51	0.33	E/S0
ATHDFS_J223238.5-605018	0.57	0.59	E/S0
ATHDFS_J223411.6-604931	0.02	0.24	Sbc
ATHDFS_J223221.3-604929	0.51	0.52	E/S0
ATHDFS_J223223.6-604923	0.34	0.52	Sbc
ATHDFS_J223301.3-604926	0.42	0.63	Sbc
ATHDFS_J223414.3-604923	0.42	0.32	E/S0
ATHDFS_J223524.8-604918A	0.78	0.74	Sbc
ATHDFS_J223524.8-604918B	...	0.92	Sbc
ATHDFS_J223413.1-604909	0.19	0.31	Scd
ATHDFS_J223107.4-604855	...	0.31	E/S0
ATHDFS_J223400.5-604903B	...	0.77	Irr
ATHDFS_J223359.4-604901	...	0.59	Irr
ATHDFS_J223543.9-604838	0.45	0.37	E/S0
ATHDFS_J223235.6-604844	...	0.61	E/S0
ATHDFS_J223452.0-604834	0.48	0.31	Sbc
ATHDFS_J223337.8-604833	0.67	0.53	Sbc
ATHDFS_J223255.7-604823	0.78	0.77	Sbc
ATHDFS_J223250.5-604814	0.74	0.59	Scd
ATHDFS_J223243.0-604758	0.60	0.71	Scd
ATHDFS_J223414.7-604753	0.03	0.26	Sbc
ATHDFS_J223217.6-604751	1.24	0.22	SB1
ATHDFS_J223417.5-604749	0.04	0.14	Scd
ATHDFS_J223226.8-604745	0.71	0.64	Sbc
ATHDFS_J223353.3-604723	2.05	...	...
ATHDFS_J223444.0-604710	...	0.-	SB1
ATHDFS_J223315.8-604707	...	0.55	E/S0
ATHDFS_J223527.8-604639A	...	0.31	E/S0
ATHDFS_J223231.6-604654	...	0.92	Sbc
ATHDFS_J223254.0-604650	...	0.59	Sbc
ATHDFS_J223305.3-604647	0.34	0.26	E/S0
ATHDFS_J223118.9-604644	1.15	0.86	Scd
ATHDFS_J223333.2-604642	0.23	0.15	E/S0
ATHDFS_J223228.5-604642	0.74	0.74	Sbc
ATHDFS_J223536.8-604632	0.03	0.25	Sbc
ATHDFS_J223330.4-604624	0.45	0.34	E/S0
ATHDFS_J223310.2-604601	...	0.47	Sbc
ATHDFS_J223342.9-604524	0.16	0.36	Sbc
ATHDFS_J223324.0-604516	0.42	0.32	E/S0
ATHDFS_J223320.1-604457	...	0.31	Scd
ATHDFS_J223443.3-604452	1.70	0.10	SB1
ATHDFS_J223311.5-604449	1.06	0.51	SB2
ATHDFS_J223319.1-604428	1.24	0.74	SB2
ATHDFS_J223210.3-604433	0.71	0.69	E/S0
ATHDFS_J223439.0-604435	0.48	0.66	Sbc
ATHDFS_J223244.1-604437	0.32	0.44	SB1

Table 11
(Continued)

ATHDF-S name	Teplitz et al. (2001) redshift	Redshift (this work)	Spectral type
ATHDFS_J223147.2-604415	0.48	0.44	E/S0
ATHDFS_J223326.3-604416	...	0.17	E/S0
ATHDFS_J223422.4-604412	0.89	...	...
ATHDFS_J223226.8-604408	0.86	0.86	Sbc
ATHDFS_J223313.9-604359	1.99	0.23	Scd
ATHDFS_J223101.3-604351	1.49	0.04	Sbc
ATHDFS_J223147.4-604338	0.60	0.29	SB2
ATHDFS_J223126.2-604337	0.01	...	...
ATHDFS_J223534.3-604328	0.64	0.53	SB1
ATHDFS_J223250.6-604336	1.11	...	...
ATHDFS_J223522.2-604326	1.87	0.21	Scd
ATHDFS_J223440.4-604309	0.34	0.35	Scd
ATHDFS_J223430.8-604310	0.34	0.35	Scd
ATHDFS_J223240.2-604306	0.51	0.33	Scd
ATHDFS_J223207.9-604305	0.74	0.53	Scd
ATHDFS_J223130.4-604232	...	0.67	E/S0
ATHDFS_J223239.0-604230	0.03	0.05	E/S0
ATHDFS_J223312.4-604227	0.57	0.41	Sbc
ATHDFS_J223437.2-604214	0.45	0.37	E/S0
ATHDFS_J223338.8-604216	1.65	0.32	Irr
ATHDFS_J223523.6-604207	0.48	0.39	E/S0
ATHDFS_J223135.8-604207	0.40	0.32	E/S0
ATHDFS_J223359.8-604155	0.10	0.08	Sbc
ATHDFS_J223255.4-604151	0.16	0.18	SB2
ATHDFS_J223158.4-604142	0.82	0.79	Sbc
ATHDFS_J223339.5-604131	...	0.33	Sbc
ATHDFS_J223224.5-604113	0.60	0.64	E/S0
ATHDFS_J223448.3-604042	0.11	0.21	Scd
ATHDFS_J223430.1-604043	0.60	0.51	Sbc
ATHDFS_J223337.5-604006	0.40	0.34	Scd
ATHDFS_J223438.0-603951	0.42	0.38	E/S0
ATHDFS_J223047.9-603933	0.57	0.44	Sbc
ATHDFS_J223220.6-603931	0.30	0.23	E/S0
ATHDFS_J223529.2-603927	0.54	0.58	E/S0
ATHDFS_J223400.2-603930	0.71	0.68	Scd
ATHDFS_J223222.7-603924	0.54	0.43	Scd
ATHDFS_J223253.7-603921	0.54	0.73	Sbc
ATHDFS_J223331.3-603914	0.48	0.38	E/S0
ATHDFS_J223123.1-603903	0.16	0.06	Sbc
ATHDFS_J223245.6-603857	...	0.75	Irr
ATHDFS_J223144.4-603858	0.32	0.26	E/S0
ATHDFS_J223153.7-603853	0.89	0.52	Irr
ATHDFS_J223450.4-603844	0.42	0.34	E/S0
ATHDFS_J223307.1-603846	0.64	0.55	Sbc
ATHDFS_J223457.3-603840	0.64	0.52	Sbc
ATHDFS_J223232.3-603842	...	0.23	E/S0
ATHDFS_J223304.6-603835	0.71	0.59	Sbc
ATHDFS_J223138.7-603818	...	0.62	Sbc
ATHDFS_J223248.2-603805	0.54	0.40	Sbc
ATHDFS_J223334.4-603804	0.54	0.56	Irr
ATHDFS_J223436.9-603754	1.29	0.97	Sbc
ATHDFS_J223254.5-603748	0.21	0.23	Sbc
ATHDFS_J223350.0-603741	...	0.61	E/S0
ATHDFS_J223232.8-603737	...	0.77	E/S0
ATHDFS_J223404.8-603732	...	0.98	Sbc
ATHDFS_J223437.7-603726	0.48	0.37	Scd
ATHDFS_J223417.1-603724	0.07	0.32	Sbc
ATHDFS_J223341.2-603724	0.82	0.88	Scd
ATHDFS_J223225.6-603717	0.54	0.45	Scd
ATHDFS_J223506.5-603700	0.34	0.05	SB2
ATHDFS_J223400.2-603653	0.12	0.08	Sbc
ATHDFS_J223525.8-603652	0.86	0.88	Sbc
ATHDFS_J223404.3-603638	0.48	0.42	E/S0
ATHDFS_J223406.7-603637	0.01	0.10	Scd
ATHDFS_J223341.9-603634	...	0.04	Scd
ATHDFS_J223451.7-603632	0.32	0.29	Sbc

Table 11
(Continued)

ATHDF-S name	Teplitz et al. (2001) redshift	Redshift (this work)	Spectral type
ATHDFS_J223316.5-603627	0.60	0.29	SB2
ATHDFS_J223526.2-603617	0.51	0.37	Sbc
ATHDFS_J223518.7-603619	...	0.12	SB1
ATHDFS_J223158.5-603614	0.51	0.42	Scd
ATHDFS_J223421.8-603603	2.05	0.22	Scd
ATHDFS_J223232.4-603542A	0.42	...	...
ATHDFS_J223232.4-603542B	0.42	...	...
ATHDFS_J223104.8-603549	0.71	0.58	Scd
ATHDFS_J223525.7-603544	0.04	0.06	Scd
ATHDFS_J223224.0-603537	...	0.17	Scd
ATHDFS_J223253.0-603539	0.74	0.58	Scd
ATHDFS_J223245.3-603537	...	0.51	Scd
ATHDFS_J223046.1-603525	0.57	0.44	Sbc
ATHDFS_J223338.8-603523	0.16	0.14	E/S0
ATHDFS_J223208.3-603519	0.45	0.36	Sbc
ATHDFS_J223344.9-603515	0.51	0.46	Scd
ATHDFS_J223524.8-603509	...	0.58	Sbc
ATHDFS_J223536.3-603506	0.89	0.96	Sbc
ATHDFS_J223549.5-603502	0.57	0.50	Sbc
ATHDFS_J223350.5-603503	...	0.98	E/S0
ATHDFS_J223541.5-603454	0.64	0.53	Sbc
ATHDFS_J223438.6-603450	0.30	0.19	E/S0
ATHDFS_J223103.2-603453	0.57	0.58	E/S0
ATHDFS_J223425.0-603452	...	0.72	SB2
ATHDFS_J223212.3-603448	0.08	0.17	Scd
ATHDFS_J223207.4-603445	0.37	0.30	E/S0
ATHDFS_J223243.3-603443	0.57	0.46	Sbc
ATHDFS_J223442.8-603433	0.57	0.30	Scd
ATHDFS_J223216.6-603434	1.15	0.83	Scd
ATHDFS_J223539.3-603424	...	0.87	Sbc
ATHDFS_J223153.2-603422	0.42	0.35	E/S0
ATHDFS_J223401.0-603424	...	0.13	E/S0
ATHDFS_J223245.5-603419	0.54	0.39	Sbc
ATHDFS_J223311.9-603417	0.42	0.64	Sbc
ATHDFS_J223434.1-603410	...	0.76	Irr
ATHDFS_J223053.2-603402	1.15	0.94	Scd
ATHDFS_J223415.0-603408	0.57	0.48	Scd
ATHDFS_J223409.7-603402	0.78	0.79	Scd
ATHDFS_J223512.7-603353	0.57	0.58	E/S0
ATHDFS_J223306.0-603350	0.17	0.30	Scd
ATHDFS_J223329.7-603352	...	0.11	SB1
ATHDFS_J223243.4-603352	1.24	0.81	SB1
ATHDFS_J223138.5-603344	...	0.24	E/S0
ATHDFS_J223420.9-603336	1.11	0.10	SB1
ATHDFS_J223225.0-603338	0.27	0.35	Scd
ATHDFS_J223513.7-603333	0.51	0.36	Sbc
ATHDFS_J223247.6-603337	0.67	0.56	Sbc
ATHDFS_J223337.5-603329	1.34	...	...
ATHDFS_J223253.1-603329	1.15	0.60	Scd
ATHDFS_J223121.6-603301	1.02	...	...
ATHDFS_J223308.6-603251	0.64	0.64	E/S0
ATHDFS_J223456.8-603251	...	0.20	SB1
ATHDFS_J223229.5-603243	...	0.75	Irr
ATHDFS_J223509.4-603235	3.06	0.22	Sbc
ATHDFS_J223142.5-603238	...	0.42	Sbc
ATHDFS_J223317.7-603235	...	0.60	E/S0
ATHDFS_J223429.9-603226	...	0.21	E/S0
ATHDFS_J223331.6-603222	0.57	0.42	Scd
ATHDFS_J223504.4-603221	0.54	0.45	Sbc
ATHDFS_J223343.5-603211	0.60	0.53	Sbc
ATHDFS_J223519.4-603157A	0.51	0.38	Sbc
ATHDFS_J223519.4-603157B	0.51	0.38	Scd
ATHDFS_J223433.9-603150	...	0.75	Irr
ATHDFS_J223449.7-603137	0.67	0.83	Sbc
ATHDFS_J223316.0-603127	0.60	0.52	Sbc
ATHDFS_J223548.9-603113	0.51	0.39	E/S0

Table 11
(Continued)

ATHDF-S name	Teplitz et al. (2001) redshift	Redshift (this work)	Spectral type
ATHDFS_J223201.4-603118	0.60	0.59	E/S0
ATHDFS_J223351.7-603117	0.67	0.49	Scd
ATHDFS_J223504.6-603109	0.08	0.05	Sbc
ATHDFS_J223415.5-603108	1.20	...	...
ATHDFS_J223447.4-603050	0.89	...	...
ATHDFS_J223404.0-603037A	1.29	...	...
ATHDFS_J223404.0-603037B	0.48	0.17	E/S0
ATHDFS_J223445.6-603032	1.34	0.98	Scd
ATHDFS_J223304.8-603031	0.54	0.40	Scd
ATHDFS_J223120.1-603025	0.51	0.37	Sbc
ATHDFS_J223241.4-603025	0.54	0.41	Scd
ATHDFS_J223440.4-603017	0.27	0.19	E/S0
ATHDFS_J223216.6-603016	0.48	0.33	Sbc
ATHDFS_J223453.7-603008	0.45	0.35	E/S0
ATHDFS_J223430.1-602959	0.01	0.28	Irr
ATHDFS_J223224.7-603005	1.44	...	...
ATHDFS_J223058.4-602952	0.82	0.82	Sbc
ATHDFS_J223530.9-602951	1.20	...	...
ATHDFS_J223534.2-602948	0.23	0.21	Sbc
ATHDFS_J223108.1-602946	...	0.32	E/S0
ATHDFS_J223316.8-602934	0.89	0.12	Scd
ATHDFS_J223513.7-602930	1.44	0.08	Sbc
ATHDFS_J223454.1-602926	0.57	0.56	E/S0
ATHDFS_J223415.3-602925	0.21	0.21	Sbc
ATHDFS_J223149.1-602924	1.24	...	...
ATHDFS_J223157.5-602919	0.67	0.36	Sbc
ATHDFS_J223447.1-602915	0.42	0.31	E/S0
ATHDFS_J223317.7-602916	1.54	0.04	Irr
ATHDFS_J223515.2-602856	0.60	0.47	Sbc
ATHDFS_J223420.1-602901	...	0.87	Sbc
ATHDFS_J223445.3-602855	1.54	...	...
ATHDFS_J223431.7-602859	0.51	0.39	Scd
ATHDFS_J223212.1-602858	0.57	0.42	Sbc
ATHDFS_J223505.0-602853	0.48	0.45	E/S0
ATHDFS_J223236.2-602855	0.34	0.40	SB2
ATHDFS_J223307.7-602853	1.44	0.54	Scd
ATHDFS_J223326.9-602850	0.02	0.02	Scd
ATHDFS_J223330.5-602849	0.21	0.35	SB2
ATHDFS_J223138.5-602834	...	0.76	Irr
ATHDFS_J223307.0-602827	...	0.07	SB2
ATHDFS_J223436.2-602821	...	0.89	Scd
ATHDFS_J223329.4-602811	...	0.24	SB1
ATHDFS_J223413.3-602808	...	0.66	Scd
ATHDFS_J223114.1-602800	...	0.75	Irr
ATHDFS_J223133.4-602755	0.60	0.46	Sbc
ATHDFS_J223443.9-602739A	0.37	0.31	E/S0
ATHDFS_J223443.9-602739B	0.37	0.31	E/S0
ATHDFS_J223443.9-602739C	0.37	0.31	E/S0
ATHDFS_J223136.1-602731	0.48	0.35	Sbc
ATHDFS_J223142.7-602719	0.60	0.47	Sbc
ATHDFS_J223332.7-602723	0.64	0.71	Scd
ATHDFS_J223227.6-602719A	0.98	0.74	SB2
ATHDFS_J223312.3-602707	...	0.86	E/S0
ATHDFS_J223432.3-602652	...	0.80	Sbc
ATHDFS_J223506.2-602647	0.64	0.46	Scd
ATHDFS_J223342.2-602639	0.51	0.60	Irr
ATHDFS_J223221.4-602629	1.20	0.70	Scd
ATHDFS_J223400.9-602633	0.37	0.31	E/S0
ATHDFS_J223212.4-602632	0.78	0.73	Sbc
ATHDFS_J223136.2-602627	0.60	0.51	Sbc
ATHDFS_J223432.6-602614	1.15	...	...
ATHDFS_J223335.3-602615	0.08	0.09	E/S0
ATHDFS_J223136.9-602610	0.60	0.49	Sbc
ATHDFS_J223442.5-602601	0.40	0.40	Irr
ATHDFS_J223148.3-602554	0.57	0.43	Scd
ATHDFS_J223357.8-602548	0.01	0.03	Scd

Table 11
(Continued)

ATHDF-S name	Teplitz et al. (2001) redshift	Redshift (this work)	Spectral type
ATHDFS_J223222.4-602532	...	0.46	E/S0
ATHDFS_J223351.2-602519	0.60	0.44	Sbc
ATHDFS_J223141.1-602506	0.19	0.31	Scd
ATHDFS_J223134.5-602457	0.37	0.56	Sbc
ATHDFS_J223317.1-602427	...	0.07	SB2
ATHDFS_J223444.9-602417	...	0.08	Scd
ATHDFS_J223436.8-602426	0.54	0.38	Scd
ATHDFS_J223245.3-602407	...	0.49	Sbc
ATHDFS_J223343.4-602348	0.14	0.20	SB2
ATHDFS_J223331.6-602307	...	0.59	E/S0
ATHDFS_J223358.9-602258	0.04	...	...
ATHDFS_J223300.5-602225	0.51	0.43	Scd
ATHDFS_J223154.6-602211	0.82	0.97	Sbc
ATHDFS_J223353.6-602136	...	0.91	Sbc
ATHDFS_J223341.1-602054	1.02	...	...
ATHDFS_J223431.4-602041	...	0.31	E/S0
ATHDFS_J223356.6-601949	0.27	0.21	E/S0
ATHDFS_J223316.0-601939	0.45	0.42	E/S0

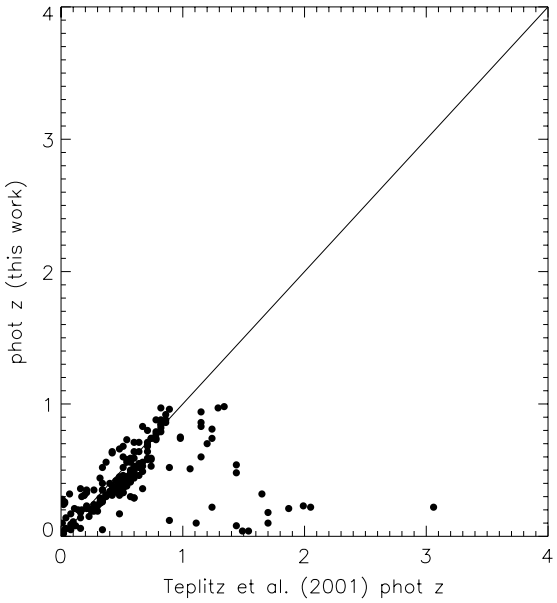

Figure 15. Comparison of Teplitz et al. (2001) and our photometric redshifts for the 209 ATHDF-S sources that have both.

radio sources ($S_{1.4\,\mathrm{GHz}} < 0.1$ mJy). This trend of fainter radio sources having fainter optical hosts was also observed by Afonso et al. (2006) (but see Barger et al. 2007).

We plot the absolute I magnitude versus redshift in Figure 18 for the 266 radio sources with redshift information. The magnitudes are k-corrected using the best-fit spectral type from the photometric redshift analysis. For six radio sources there was a 2dF spectroscopic redshift but no photometric type. The k-correction in these cases was determined from a starburst template for the 2dF emission line galaxies (two total) and an E/S0 template for the 2dF absorption line galaxies (two total). A further two cases were high redshift ($z > 2$) 2dF broadline emitting quasars, which we k-corrected with a QSO composite template from Francis et al. (1991). The approximate I magnitude limit of 23.5 is shown by the solid line in Figure 18. The host galaxies span a small range in absolute magnitude across the redshift range $0 < z < 1$. We find that the median absolute I magnitude for $z < 0.5$ sources is -21.7, while the median absolute I magnitude for sources at $0.5 < z < 1.0$ is -22.3. So there may be a trend toward these radio sources having brighter host galaxies at $0.5 < z < 1.0$, but this trend is very weak.

We show absolute I magnitude versus 1.4 GHz radio power for all radio sources with redshift information in Figure 19. The majority of the radio sources (∼80%) lie in the magnitude range -20 to -24. This corresponds to 1.6 dex in luminosity. In comparison, the radio powers have a wider range of luminosities (about 2 dex encompasses 80% of the sources). The higher redshift sources must have higher radio powers, but the median absolute I magnitude does not change noticeably with redshift (Figure 18). So the optical properties of the host galaxies are not changing as fast as the radio power of the host galaxies (see Barger et al. 2007).

In Figure 20 we plot the restframe $B - I$ colors of the optically identified radio sources in our sample against 1.4 GHz flux density and redshift. The solid, dotted, and dashed lines in Figure 20 show the restframe colors of a Coleman et al. (1980) E/S0, Sbc, and Irr galaxy, respectively. The host galaxies have colors that span the range between E/S0 to Irr, but have a median color that is Sbc like. We find little variation in the median color of the host galaxies with either flux density or redshift. Smolčić et al. (2008) also find no change in the rest frame colors of sub–mJy radio sources out to redshift $z = 1.3$. This supports the suggestion that the host galaxies of faint radio sources are drawn from the same population as that of bright radio sources (see Barger et al. 2007).

5.2. Radio-to-Optical Ratios

The radio-to-optical ratio of a radio source can give clues to the nature of the radio emission and it has traditionally been used to determine the "radio loudness" of radio sources (Kellermann et al. 1989). While optically selected samples of quasars have been found to have a wide range of radio flux densities, and thus radio-to-optical ratios (Sramek & Weedman 1980; Condon et al. 1981), it has been suggested that the distribution of this ratio is bimodal (e.g., Kellermann et al. 1989; Stocke et al. 1992). These authors find a dip in the distribution of 5 GHz to B-band flux density ratios at $3 < r = S_{5\,\mathrm{GHz}}/S_{B-\mathrm{band}} < 30$, and formally classify radio sources as radio loud if they have $r > 10$.

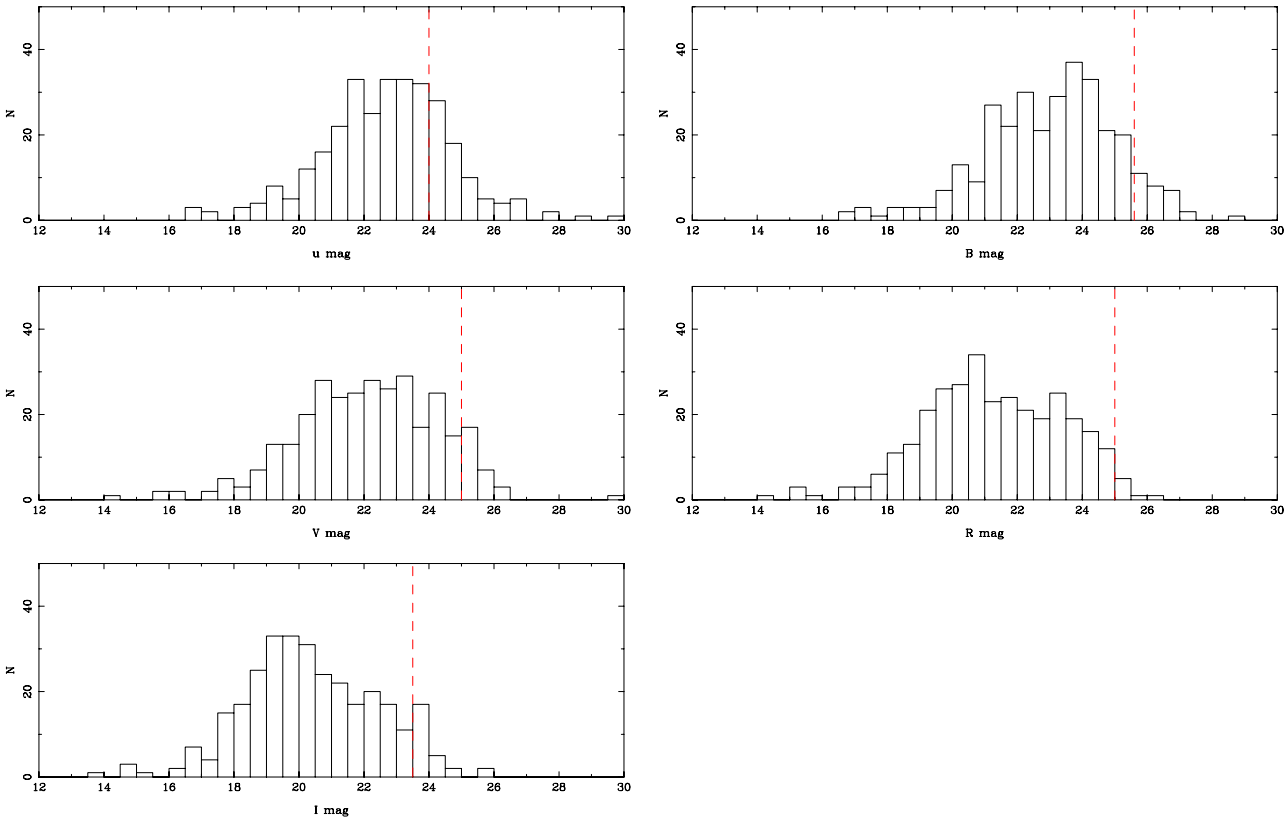

Figure 16. *uBVRI* magnitude distribution of the 315 ATHDF-S sources with CTIO counterparts.
(A color version of this figure is available in the online journal)

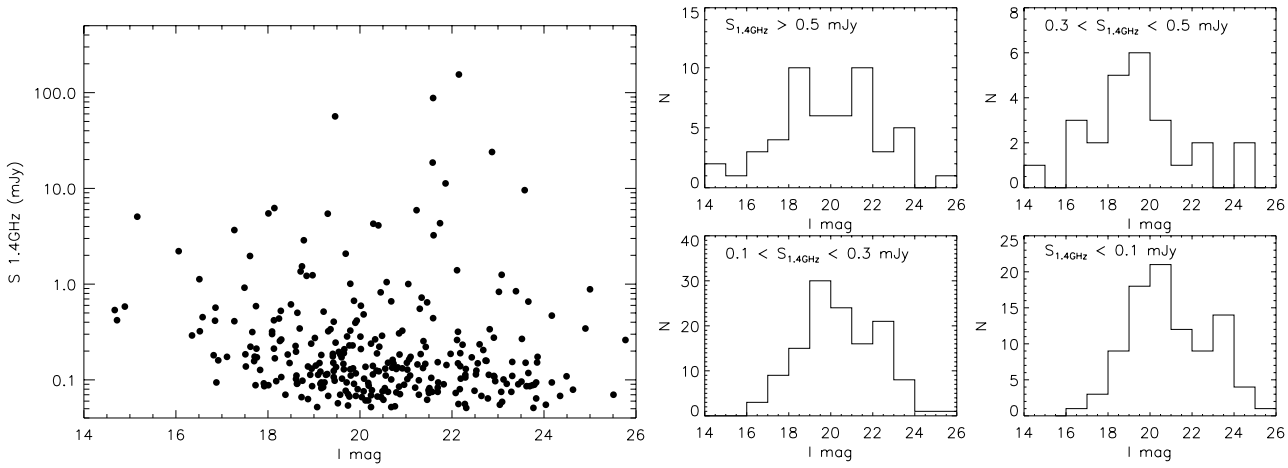

Figure 17. Left panel: the 1.4 GHz flux density versus I magnitude for the radio sources detected in the CTIO I-band image. Right panel: the I magnitude distributions for the radio sources for flux density bins as shown.

The bimodality of radio loudness is still controversial, though, with White et al. (2000) claiming no bimodality is seen for a radio-selected sample of optically bright quasars from the FIRST Bright Quasar Survey. However, Ivezić et al. (2002) combined the FIRST survey with deeper SDSS data and found evidence for a bimodality with a minimum in the radio-to-optical ratio between 1 and 10. Ivezić et al. (2002) claim that the FIRST Bright Quasar Survey was biased to radio-intermediate sources with ratios between 1 and 10 because of the brighter $I \lesssim 18$ limit and hence no bimodality was observed. Moreover, a study of the nuclear region of local Seyferts has found that 60% of them meet the radio-loud $r > 10$ criterion, suggesting that, after removing the effects of the diluting host galaxy, most Seyferts are not radio quiet (Ho & Peng 2001).

We plot the observed radio-to-I-band flux density ratio against redshift in Figure 21. The I-band was selected as it is the reddest filter and hence covers the restframe optical regime to the highest redshift. Marked in Figure 21 are ratios from the radio-loud and radio-quiet QSOs from Elvis et al. (1994). We also overplot tracks from local starbursts Arp220 and M82, which have star-formation rates of several hundred and tens of $M_{\odot}$ yr^{-1}, respectively. The radio-to-optical ratio tracks for

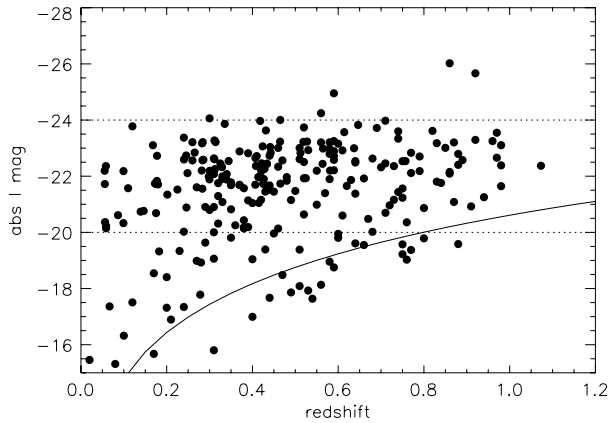

Figure 18. Absolute I-band magnitude versus redshift for the 266 radio sources with redshift information. The solid line approximates the limit of the optical survey ($I = 23.5$). The dotted lines show the range in magnitude which encompasses about 80% of the radio sources.

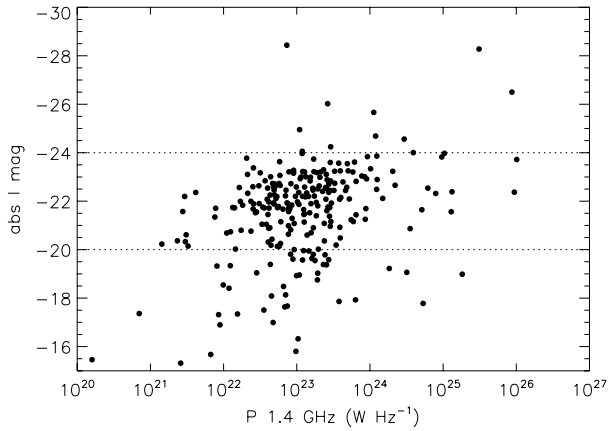

Figure 19. Absolute I-band magnitude versus radio power, P 1.4 GHz, for the 266 radio sources with redshift information. The dotted lines show the range in magnitude which encompasses about 80% of the radio sources.

the starbursts cover the intermediate range of 1–10. We find that the majority of the optically detected radio sources have radio-to-optical ratios in the range 1–100, with a median of $S_{1.4\,\mathrm{GHz}}/S_{I-\mathrm{band}} = 10.6$.

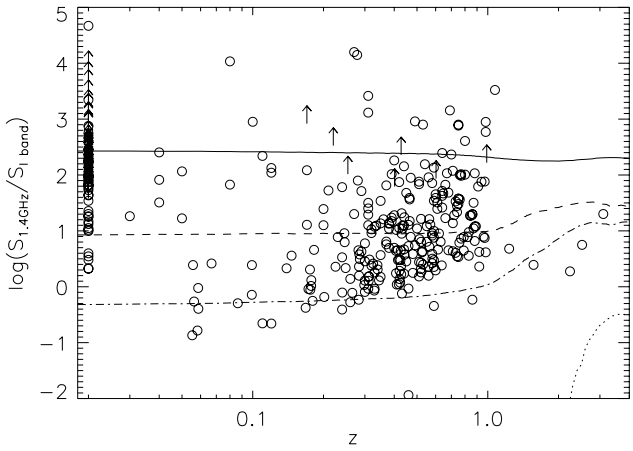

Figure 21. Radio-to-optical flux density ratio for sources in the ATHDF-S, plotted against redshift. The arrows mark lower limits of ATHDF-S sources not detected in the I-band imaging. Sources without a redshift are plotted at $z = 0.02$. The tracks for a radio loud (black solid line) and radio quiet (dotted line) from Elvis et al. (1994) are plotted for comparison. Also plotted are the ratios from prototypical starbursts Arp220 (dashed line) and M82 (dot-dashed line).

Care must be taken when interpreting the radio-to-optical ratio. At high redshifts we observe objects at a different cosmological epoch, so they may have broadband spectral energy distribution (SED) properties which differ from local objects. For instance, there is evidence that high redshift starbursts and ultraluminous infrared galaxies (ULIRGs) have SEDs that differ from local analogs (Pope et al. 2006; Huynh et al. 2007b). Also, sources at earlier epochs may be more dust obscured, which would increase the radio-to-optical ratio. The tracks in Figure 21 are therefore a rough guide only. A further complicating factor is that AGNs have variable luminosities. The luminosity of an AGN can change on timescales of minutes (X-ray) to months (radio/optical/IR) (e.g. Hawkins 2002). The effect of variability in the radio should be reduced since the radio observations were taken over a period of 3 years and any variability is therefore diluted. The optical data, however, was obtained over a period of only 3 days.

Because of these caveats we choose a conservative approach to using the radio-to-optical ratio as a radio-loudness parameter.

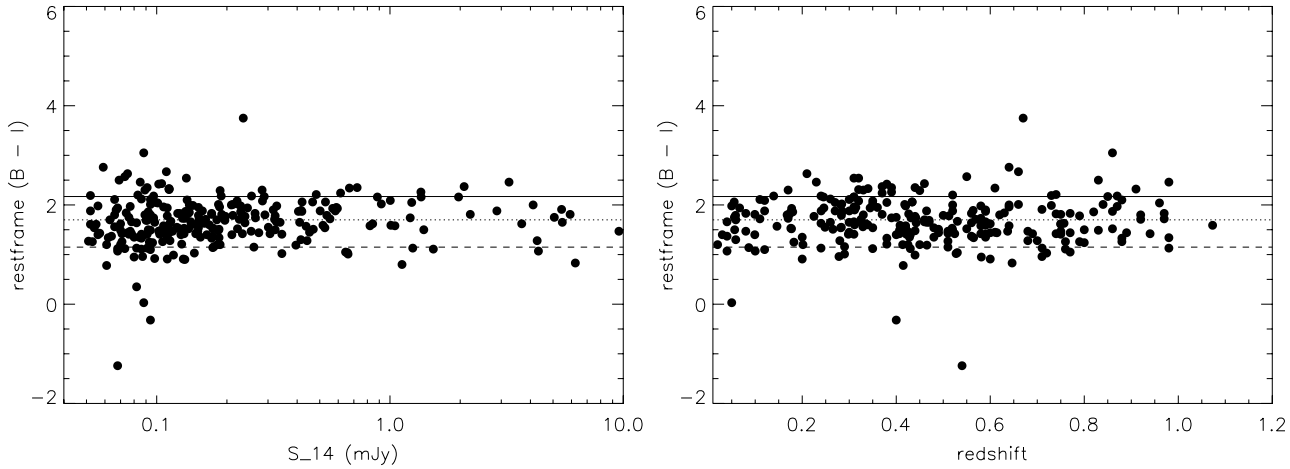

Figure 20. Left panel: the 1.4 GHz flux density versus restframe ($B - I$) color for the 266 radio sources with redshift information. The solid, dotted, and dashed lines show the restframe colors of an E/S0, Sbc and Irr galaxy (Coleman et al. 1980), respectively. Right panel: redshift versus restframe ($B - I$) color for the 266 radio sources with redshift information. The lines are as for the left panel.

Table 12
Summary of ATHDF-S Sources Deemed Radio Loud from the Radio-to-Optical Ratio

ATHDF-S name	$S_{1.4\,\mathrm{GHz}}$	I mag	R_I
ATHDF-S_J223353.9−605452	5.918	21.23	2.88
ATHDF-S_J223214.8−605430	18.601	21.58	3.52
ATHDF-S_J223448.4−605417	1.396	22.11	2.61
ATHDF-S_J223203.0−605242A	87.888	21.59	4.20
ATHDF-S_J223107.4−604855	11.272	21.86	3.42
ATHDF-S_J223320.1−604457	0.344	24.90	3.12
ATHDF-S_J223210.3−604433	56.513	19.46	3.16
ATHDF-S_J223534.3−604328	0.657	23.66	2.90
ATHDF-S_J223355.6−604315	154.700	22.15	4.67
ATHDF-S_J223123.1−603903	23.988	22.87	4.15
ATHDF-S_J223245.6−603857	0.843	23.39	2.90
ATHDF-S_J223404.8−603732	3.238	21.60	2.77
ATHDF-S_J223343.7−603651	0.070	25.51	2.67
ATHDF-S_J223350.5−603503	1.252	23.08	2.95
ATHDF-S_J223420.9−603336	4.328	21.74	2.95
ATHDF-S_J223212.9−603234A	2.816	22.02	2.88
ATHDF-S_J223212.9−603234B	1.466	22.02	2.59
ATHDF-S_J223113.5−603147	0.831	23.02	2.75
ATHDF-S_J223329.1−602933	0.261	25.77	3.34
ATHDF-S_J223444.9−602417	9.581	23.58	4.03
ATHDF-S_J223245.3−602407	0.469	24.17	2.96
ATHDF-S_J223303.6−605751	0.508	>23.5	>2.53
ATHDF-S_J223410.5−605545A	2.106	>23.5	>3.14
ATHDF-S_J223410.5−605545B	2.443	>23.5	>3.21
ATHDF-S_J223308.5−605544	3.643	>23.5	>3.38
ATHDF-S_J223317.5−605416A	7.754	>23.5	>3.71
ATHDF-S_J223317.5−605416B	5.570	>23.5	>3.57
ATHDF-S_J223403.1−605101	12.043	>23.5	>3.90
ATHDF-S_J223454.0−604904	0.483	>23.5	>2.50
ATHDF-S_J223527.8−604639B	1.423	>23.5	>2.97
ATHDF-S_J223319.1−604348	1.085	>23.5	>2.86
ATHDF-S_J223427.3−604258	0.571	>23.5	>2.58
ATHDF-S_J223417.8−604009	1.502	>23.5	>3.00
ATHDF-S_J223429.9−603629	0.671	>23.5	>2.65
ATHDF-S_J223224.0−603537	1.259	>23.5	>2.92
ATHDF-S_J223258.5−603346	1.010	>23.5	>2.82
ATHDF-S_J223509.5−603257	0.980	>23.5	>2.81
ATHDF-S_J223537.7−603013	2.860	>23.5	>3.28
ATHDF-S_J223236.5−603000	1.507	>23.5	>3.00
ATHDF-S_J223355.5−602956	1.534	>23.5	>3.01
ATHDF-S_J223140.6−602924	4.962	>23.5	>3.52
ATHDF-S_J223117.4−602850	7.756	>23.5	>3.71
ATHDF-S_J223306.6−602425	1.949	>23.5	>3.11
ATHDF-S_J223410.2−602324	0.582	>23.5	>2.58

We class sources as radio-loud AGNs if they have $R_I = \log(S_{1.4\,\mathrm{GHz}}/S_{I-\mathrm{band}}) > 2.5$. A source exceeding this ratio always lies above the radio-loud QSO track for redshifts 0–5 (Figure 21). Using this criterion, we identify 44 sources as radio-loud AGNs, including the sources with only limits in I magnitude. These sources are listed in Table 12.

One interesting source classified as radio loud is ATHDF-S_J223343.7−603651 which has a 1.4 GHz flux density of 0.070 mJy. This faint source is at the detection limit of the CTIO images, and we have no redshift information for it. In Paper III we quote a radio spectral index of $\alpha_{1.4\,\mathrm{GHz}}^{2.5\,\mathrm{GHz}} = -1.14 \pm 0.39$ for this source and identified it as an ultra-steep spectrum radio source. The radio-loud classification of this source is consistent with it being a high redshift radio galaxy.

The distribution of the radio-to-optical ratio of the I-band-identified sources is shown in Figure 22. The R_I distribution of sources brighter than 1 mJy shows signs of bimodality, in accordance with Ivezić et al. (2002). Although the small number of sources makes it difficult to accurately determine the shape of the radio-to-optical ratio distribution, we find the number of radio bright sources peaks at $R_I > 2$ and has a dip at $0 < R_I < 1$. If we then assume that most of the optically selected AGNs in the HDF-S are not detected in the radio, then these undetected optical AGNs have $R_I < 0$ and the unobserved part of the R_I distribution must rise for $R_I < 0$. This is inconsistent with White et al. (2000), but this previous work only had shallow imaging ($I \sim$ 18th mag compared to our $I = 23.5$ limit). Our sample is radio selected, however, so a complete radio survey of a sample of optically selected AGNs is needed to confirm the radio-loud/radio-quiet bimodality of the AGNs. Sixty percent (31/51) of these radio bright sources have ratios greater than $R_I > 2.5$, meeting our conservative radio-loud criterion.

For the full sample, the radio-to-optical ratio shows no sign of bimodality and has a roughly Gaussian distribution with a peak at $R_I = 0.5$–1 (Figure 22). However, we only have I-band detections for 66% of the sources, and deeper optical imaging is needed to determine the distribution at $R_I > 2$. The faint radio sources are more radio quiet than bright radio sources (as expected). The R_I distribution for the fainter radio sources also shows an extended tail at high ratios, which means we cannot rule out low-luminosity AGNs in this population. We posit that there may be a lack of sources with ratios in the region $0 < R_I < 1$ at higher radio flux densities, but starbursts and radio-intermediate AGNs increase in number as fainter radio flux densities are probed, so the gap in the R_I distribution between 0 and 1 is filled (see Figure 23). We also note that there is a subsample of radio sources which are undetected in the I-band with high radio-to-optical ratios ($R_I > 1.5$), which are the optically faint microjansky sources which are discussed in Section 2.3.3. Their ratios imply that they are radio-loud AGNs or starbursts with large dust obscuration.

5.3. Radio Power and Redshift Distribution

Radio luminosities for the ATHDF-S sources are calculated with the redshifts presented in this paper. In Figure 24, we plot the 1.4 GHz radio luminosity of the ATHDF-S radio sources against redshift for the spectroscopic and photometric redshift samples. The galaxies classed as star-forming from 2dF spectra have luminosities in the range $\log(P_{1.4\,\mathrm{GHz}}) \sim 20.5$–$23.5$ W Hz^{-1}. The early-type galaxies have larger radio powers of $\log(P_{1.4\,\mathrm{GHz}}) \sim 21.5$–$24.5$ W Hz^{-1}. This is expected as the radio emission from early-type galaxies is driven by a weak AGN, which is more radio powerful than star-formation processes. Also as expected, the broadline AGNs are the most powerful radio sources ($\log(P_{1.4\,\mathrm{GHz}}) \sim 23$–$26$ W Hz^{-1}). Consistent with Smolčić et al. (2008), we find significant overlap in the radio powers of the star-forming and early galaxy types, and even broadline AGNs can have similar radio powers to the most powerful starbursts. This means that radio power alone cannot be used as a discriminator of source types.

The redshift distribution of our sources with spectroscopic redshifts is shown in Figure 25. The median redshift of the whole spectroscopic sample is 0.34. The star-forming galaxies are at similar redshifts to the early-type galaxies, with median redshifts of 0.28 and 0.31 for the star-forming and early-type samples, respectively. We note that there is a lack of both spectroscopic star-forming and early-type galaxies at $z > 0.5$ because of our survey sensitivity limit. The solid line in Figure 24, which marks the radio power sensitivity of our survey,

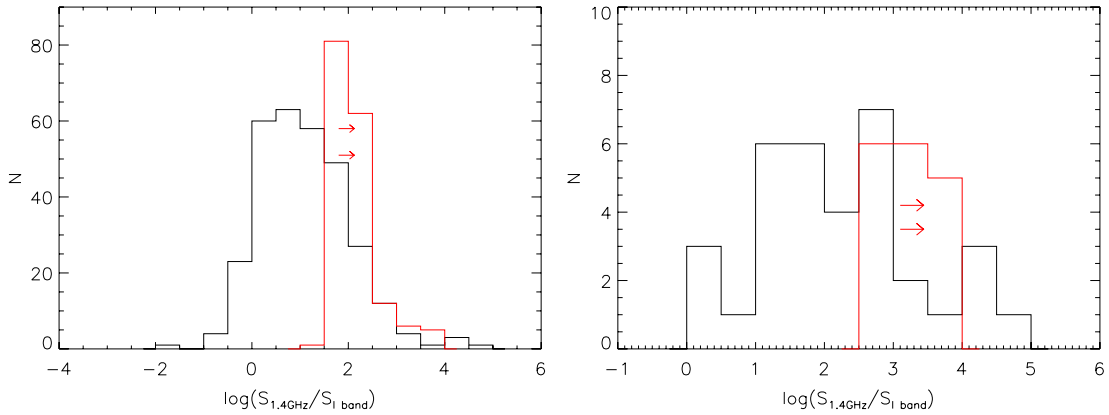

Figure 22. Radio-to-optical ratio (R_I) distribution of the ATHDF-S sources with CTIO I-band counterparts (black solid line). The lower limit of R_I for sources not detected in the I-band are determined using the nominal CTIO I-band limit of 23.5 mag. These lower limits are shown as the red histogram. Left: full ATHDF-S sample. Right: radio bright ($S_{1.4\,\mathrm{GHz}} > 1$ mJy) sample.

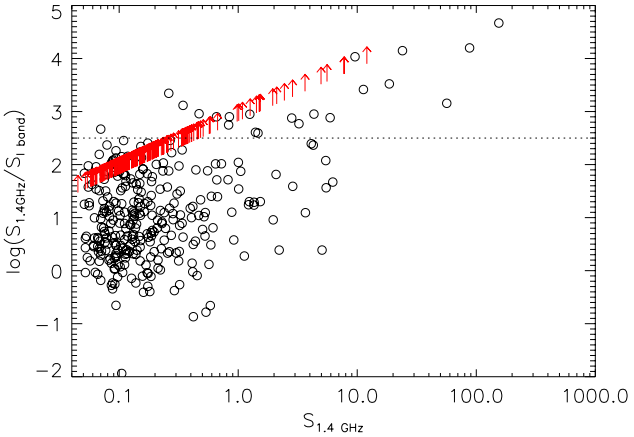

Figure 23. Radio-to-optical ratio (R_I) plotted against 1.4 GHz flux density. The dotted line marks our radio-loud criterion of $R_I > 2.5$. The bright ($S_{1.4\,\mathrm{GHz}} > 1$ mJy) radio sources have higher ratios than the faint sub-mJy radio sources, which have intermediate radio-to-optical ratios of $0 < R_I < 1$. There is a sizeable number of radio sources at the 0.1 mJy level with $R_I \gtrsim 2$, as indicated by the radio sources not detected in the I-band imaging (arrows), and some of these may be radio-loud AGNs.

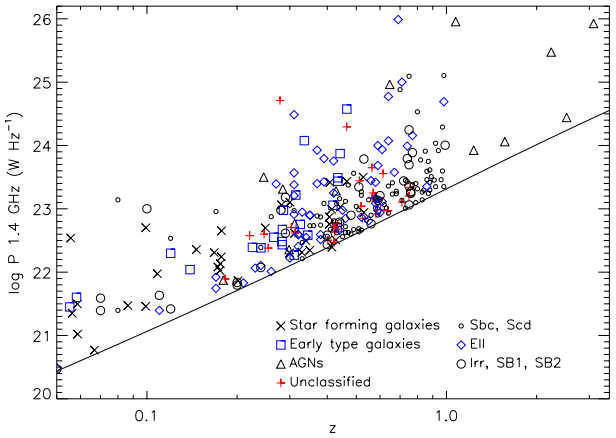

Figure 24. 1.4 GHz luminosity (W Hz^{-1}) of all our radio sources that have redshifts, as a function of redshift. The symbols are as shown in the legend. The left column of the legend is for sources with 2dF spectroscopic redshifts and the right column for sources with photometric redshifts. The solid line marks the detection limit of 0.050 mJy.

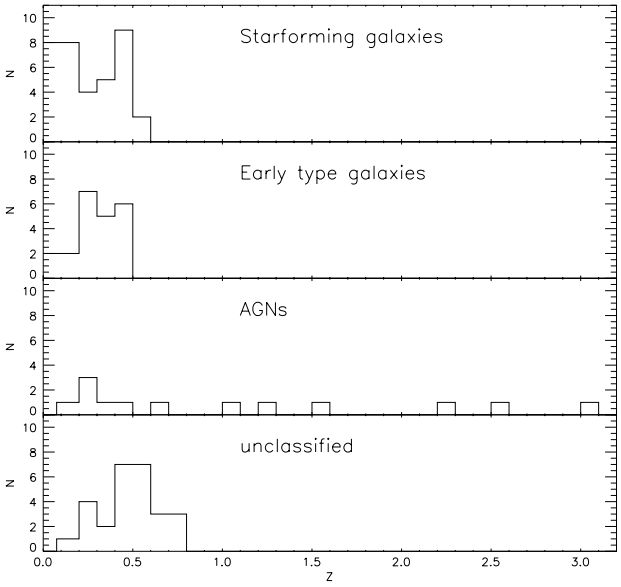

Figure 25. Redshift distribution of our radio sources with 2dF spectra. Different spectral classes are drawn separately. From top to bottom: star-forming galaxies, early-type galaxies, AGNs, and unclassified. See the text for description of classes.

shows how our radio survey becomes increasingly insensitive to sources with star-forming and early-type radio powers as higher redshifts are probed. The broadline AGNs are detected at both low and moderate redshifts, but only the most powerful ($\log(P_{1.4\,\mathrm{GHz}}) \gtrsim 24$) are detected at $z > 1$. The highest redshift source is a broadline AGN estimated to be at $z = 3.1$. Finally we note that the unclassified sources are at greater redshifts than the star-forming or early-type galaxies, with a median redshift of 0.46. The greater distance to these sources make them on average fainter in the optical, and thus the spectroscopy of these sources is of lower quality, as expected.

In Figure 26 we show the photometric redshift distribution of our sources, sorted into best-fit template types. The late type galaxies, Sbc and Scd, show a Gaussian-like distribution with a peak at $z = 0.35$ and an extended tail. The distribution of the early-type galaxies is similar, with a peak also at $z = 0.35$. Again we argue that the decline in the number of sources in these two samples for $z > 0.5$ is probably because of our survey

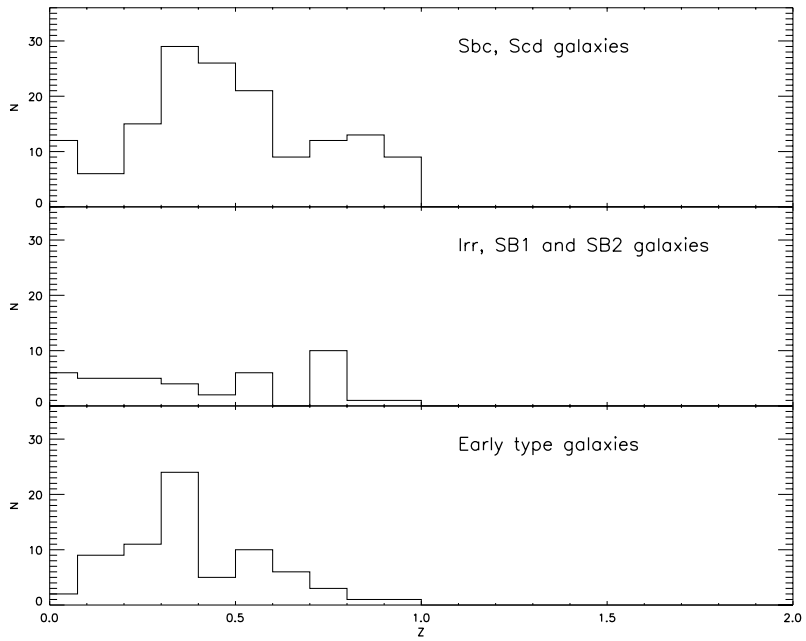

Figure 26. Redshift distribution of our radio sources with photometric redshifts. Samples with different best-fit templates are drawn separately. From top to bottom: late-type galaxies (Sbc and Scd), starbursts/irregulars, and early-type galaxies. See the text for description of classes.

sensitivity. The starbursts and irregulars appear to have a more uniform distribution than the early- or late-type samples.

6. SUMMARY

We have cross-matched the ATHDF-S radio sources with optical imaging from CTIO. We find 306/465 (66%) of the radio sources which lie within the region covered by the CTIO imaging have counterparts to $I = 23.5$.

The *HST* imaging was also used to search for optical counterparts to our radio sources. The *HST* imaging reaches a sensitivity approximately 2.5 mag deeper than the CTIO imaging. This identifies a further ∼12% of sources in the *HST* region. Thus, the identification rate of sub-mJy radio sources to I = 26.0 is estimated to be 79%. A sizable proportion (∼20%) are fainter than this and remain optically unidentified. These optically faint microjansky sources, also found in other radio surveys, are thought to be a mix of starbursts at $1 < z < 3$ and high redshift obscured AGNs.

We have presented spectroscopic redshifts derived from 2dF spectra for 98 of the radio sources. Where the spectra is of sufficient quality, the sources have been classified as early-type, star-forming, Seyfert, or broadline AGNs. The spectroscopic sample consists of 22% early type, 37% late type, and 13% Seyferts or broadline AGNs. The median redshift of the sample is $z = 0.34$ and a broadline AGN at $z = 3.1$ has been discovered. Photometric redshifts from five-band CTIO photometry have also been calculated for 264 ATHDF-S sources. A total of 56% (266/473) of the radio sources have redshift information.

Using the available optical information, our main results are as follows:

The observed I-band magnitude of $S_{1.4\,\mathrm{GHz}} > 0.5$ mJy radio sources is 0.8 mag brighter than the faintest radio sources ($S_{1.4\,\mathrm{GHz}} < 0.1$ mJy).

The median restframe $B - I$ color of the optical hosts is consistent with that of a Sbc galaxy.

There is little variation in the restframe optical colors of the host galaxies with redshift (to $z \sim 1$) or 1.4 GHz flux density. This suggests that faint and bright radio sources have similar host galaxies and that the host galaxies do not evolve much with redshift. It is also further evidence that there is a significant fraction of low-luminosity or radio-quiet AGNs in the sub-mJy radio population.

Using a conservative radio-to-optical flux density ratio, we conclude that 44 of the sources are radio loud and most likely powered by an AGN. We find that 61% (31/51) of bright radio sources ($S_{1.4\,\mathrm{GHz}} > 1$ mJy) have a radio-to-optical ratio that fits the radio-loud criterion.

The distribution of the radio-to-optical ratios of the bright ($S_{1.4\,\mathrm{GHz}}$) radio sources is consistent with a radio-loud/radio-quiet bimodality. However, complete radio observations of an optically selected sample of AGNs are required to confirm the dichotomy. We find no evidence for the radio-loud/radio-quiet bimodality in the full ATHDF-S sample, which we believe is due to radio-intermediate starbursts, and low-luminosity AGNs becoming more numerous at sub-mJy flux density levels.

The mid-IR wavelengths can be good discriminators of star-formation versus AGN emission (Lacy et al. 2004; Stern et al. 2005). The HDF-S has been observed in the IR by the *Spitzer Space Telescope*. Future papers in this series will present the *Spitzer* identifications of the ATHDF-S radio sources to further investigate the nature of faint radio sources.

M.T.H. would like to thank Nick Seymour for useful discussions. A.F.S. acknowledges support from MEC Project AYA2006-14056 and a "Ramón y Cajal" research contract. The Australia Telescope Compact Array is part of the Australia Telescope, which is funded by the Commonwealth of Australia for operation as a National Facility managed by the CSIRO.

REFERENCES

Afonso, J., Mobasher, B., Koekemoer, A., Norris, R. P., & Cram, L. 2006, AJ, 131, 1216
Alexander, D. M., Brandt, W. N., Hornschemeier, A. E., Garmire, G. P., Schneider, D. P., Bauer, F. E., & Griffiths, R. E. 2001, AJ, 122, 2156
Barger, A. J., Cowie, L. L., & Richards, E. A. 2000, AJ, 119, 2092
Barger, A. J., Cowie, L. L., & Wang, W.-H. 2007, ApJ, 654, 764
Bertin, E., & Arnouts, S. 1996, A&AS, 117, 393
Bruzual, A. G., & Charlot, S. 1993, ApJ, 405, 538
Casertano, S., et al. 2000, AJ, 120, 2747
Chapman, S. C., Richards, E. A., Lewis, G. F., Wilson, G., & Barger, A. J. 2001, ApJ, 548, L147
Chapman, S. C., et al. 2003, ApJ, 585, 57
Coleman, G. D., Wu, C.-C., & Weedman, D. W. 1980, ApJS, 43, 393
Colless, M., et al. 2001, MNRAS, 328, 1039
Condon, J. J. 1984, ApJ, 287, 461
Condon, J. J. 1989, ApJ, 338, 13
Condon, J. J., Odell, S. L., Puschell, J. J., & Stein, W. A. 1981, ApJ, 246, 624
Croton, D. J., et al. 2006, MNRAS, 365, 11
Elvis, M., et al. 1994, ApJS, 95, 1
Fernández-Soto, A., Lanzetta, K. M., & Yahil, A. 1999, ApJ, 513, 34
Francis, P. J., Hewett, P. C., Foltz, C. B., Chaffee, F. H., Weymann, R. J., & Morris, S. L. 1991, ApJ, 373, 465
Gardner, J. P., et al. 2000, AJ, 119, 486
Glazebrook, K., Verma, A., Boyle, B., Oliver, S., Mann, R. G., & Monbleau, D. 2006, AJ, 131, 2383
Hawkins, M. R. S. 2002, MNRAS, 329, 76
Ho, L. C., & Peng, C. Y. 2001, ApJ, 555, 650
Huynh, M. T., Jackson, C. A., & Norris, R. P. 2007a, AJ, 133, 1331
Huynh, M. T., Jackson, C. A., Norris, R. P., & Prandoni, I. 2005, AJ, 130, 1373
Huynh, M. T., Pope, A., Frayer, D. T., & Scott, D. 2007b, ApJ, 659, 305
Ivezić, Ž., et al. 2002, AJ, 124, 2364
Jarvis, M. J., & Rawlings, S. 2004, New Astron. Rev., 48, 1173
Kellermann, K. I., Sramek, R., Schmidt, M., Shaffer, D. B., & Green, R. 1989, AJ, 98, 1195
Kewley, L. J., Heisler, C. A., Dopita, M. A., & Lumsden, S. 2001, ApJS, 132, 37
Kinney, A. L., Calzetti, D., Bohlin, R. C., McQuade, K., Storchi-Bergmann, T., & Schmitt, H. R. 1996, ApJ, 467, 38
Kormendy, J., & Richstone, D. 1995, ARA&A, 33, 581
Labbé, I., et al. 2003, AJ, 125, 1107
Lacy, M., et al. 2004, ApJS, 154, 166
Landolt, A. U. 1992, AJ, 104, 340
Lucas, R. A., et al. 2003, AJ, 125, 398
Muxlow, T. W. B., et al. 2005, MNRAS, 358, 1159
Norris, R. P., et al. 2005, AJ, 130, 1358
Palunas, P., et al. 2000, ApJ, 541, 61
Pope, A., et al. 2006, MNRAS, 370, 1185
Richards, E. A., Fomalont, E. B., Kellermann, K. I., Windhorst, R. A., Partridge, R. B., Cowie, L. L., & Barger, A. J. 1999, ApJ, 526, L73
Rowan-Robinson, M., Benn, C. R., Lawrence, A., McMahon, R. G., & Broadhurst, T. J. 1993, MNRAS, 263, 123
Rudnick, G., et al. 2001, AJ, 122, 2205
Sawicki, M., & Mallén-Ornelas, G. 2003, AJ, 126, 1208
Sealey, K. M., Drinkwater, M. J., & Webb, J. K. 1998, ApJ, 499, L135
Seymour, N., McHardy, I. M., & Gunn, K. F. 2004, MNRAS, 352, 131
Seymour, N., et al. 2008, MNRAS, 386, 1695
Simpson, C., et al. 2006, MNRAS, 372, 741
Smolčić, V., et al. 2008, ApJ, in press (arXiv:0803.0997)
Sramek, R. A., & Weedman, D. W. 1980, ApJ, 238, 435
Stern, D., et al. 2005, ApJ, 631, 163
Stocke, J. T., Morris, S. L., Weymann, R. J., & Foltz, C. B. 1992, ApJ, 396, 487
Teplitz, H. I., Hill, R. S., Malumuth, E. M., Collins, N. R., Gardner, J. P., Palunas, P., & Woodgate, B. E. 2001, ApJ, 548, 127
Vanzella, E., et al. 2002, A&A, 396, 847
Wall, J. V., Benn, C. R., Grueff, G., & Vigotti, M. 1986, Highlights in Astronomy, 7, 345
White, R. L., et al. 2000, ApJS, 126, 133
Williams, R. E., et al. 2000, AJ, 120, 2735
Windhorst, R. A., Miley, G. K., Owen, F. N., Kron, R. G., & Koo, D. C. 1985, ApJ, 289, 494
Yahata, N., Lanzetta, K. M., Chen, H., Fernández-Soto, A., Pascarelle, S. M., Yahil, A., & Puetter, R. C. 2000, ApJ, 538, 493